Materials & Design 257 (2025) 114421

Contents lists available at ScienceDirect

Materials & Design

journal homepage: www.elsevier.com/locate/matdes

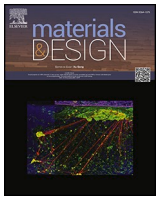

Crystallographic texture and precipitation control via double austenitization in high-performance tool steel

Hamza Sofiane Meddas [a,*], Muftah Zorgani [a], Majid Heidari [b], Mousa Javidani [c], Tom Levasseur [b], Mohammad Jahazi [a]

[a] Department of Mechanical Engineering, École de Technologie Supérieure (ÉTS), Montréal, QC H3C 1K3, Canada
[b] DK SPEC Company, 1060, Chemin Olivier, St-Nicolas, Lévis, QC G7A 2M8, Canada
[c] Department of Applied Science, University of Quebec at Chicoutimi, Saguenay, QC G7H 2B1, Canada

ARTICLE INFO

Keywords:
Tool steel
Martensite
Variant pair
Toughness
$M_{23}C_6$ precipitation

ABSTRACT

In the present work, the toughness and wear resistance of AISI A8 cold work high-strength tool steel were improved through the design of a specific double austenitization and tempering heat treatment. The treatment resulted in 80 % improvement in impact toughness and 10 % improvement in wear resistance. A combination of high-resolution dilatometry and scanning electron microscopy, including phase compositional and crystallographic analysis, was used to identify the microstructural changes. The findings were analyzed in terms of the influence of the proposed heat treatment on the refinement of the as-quenched martensite substructure and the fraction of high-angle grain boundaries (V1/V2, V1/V3 and V1/V6) variant pairs and the fraction of low-angle grain boundaries (V1/V4) pairs. Notably, block width analysis revealed that in the double austenitization treatment, block width appeared insensitive to prior austenite grain size variations. Additionally, the kinetics of the $M_{23}C_6$ secondary carbides precipitation during isothermal tempering at 520 °C was investigated and modeled. Results demonstrate that the redistribution of carbon in solid solution is the critical microstructural parameter influencing the variant selection and the homogenous precipitation of spherical carbides. The underlying micro-mechanisms responsible for such improvement were identified and their contributions documented and quantified.

1. Introduction

Cold work tool steels, an important subclass of tool steels, include both low and high alloy grades and are specifically designed for applications involving tooling and cutting operations conducted at ambient temperatures where thermal effects on material performance are minimal [1,2]. AISI A8, a prominent air-hardened tool steel, is extensively utilized in industrial manufacturing environments where dimensional stability and performance under mechanical stress are required [3]. The final microstructure consists of tempered lath martensite and tempering $M_{23}C_6$ carbides where M is mainly Chromium [4]. These steels are generally produced via conventional casting and forging, followed by annealing, quenching, and tempering heat treatments [2]. Despite their widespread applications, these steels frequently encounter significant challenges, including premature tool failure characterized by edge recession [5] and chipping mechanisms [6]. These failure modes substantially limit the operational efficiency and economic viability of cutting tools, highlighting the urgent need for advanced material processing strategies. Toughness is essential to prevent chipping and cracking under impact loads, while wear resistance is vital to maintain dimensional stability and extend the tool's lifespan under abrasive conditions.

Previous studies [7,8] have indicated the critical role of microstructure in determining the mechanical properties of tool steels, particularly in terms of toughness and wear resistance. Heydari et al. [9] recently analyzed the fracture behavior of a wrought tool steel and showed that the crack path was driven by both, the presence of sub-grain boundaries in the matrix, and by the carbide distribution alongside the matrix. The crack diverts from one carbide particle to another, propagating through the matrix. Similarly, Randelius [8] observed that the size of the precipitates influenced crack initiation at the matrix/precipitate interfaces, while crack propagation was governed by the toughness of the matrix.

The toughening and strengthening mechanisms implicated in the

* Corresponding author.
E-mail address: hamza-sofiane.meddas.1@ens.etsmtl.ca (H.S. Meddas).

https://doi.org/10.1016/j.matdes.2025.114421
Received 5 March 2025; Received in revised form 6 July 2025; Accepted 17 July 2025
Available online 20 July 2025

martensite matrix are often discussed in terms of the hierarchically arranged substructures (packets and blocks of individual martensite laths) within the prior austenite grains (PAGs). Transformation path from austenite to lath martensite follows a near Kurdjumov-Sachs (K-S) orientation relationship (OR) [10]. Extensive studies [11,12,13] have been focusing on the behavior of lath martensite, and it has been reported that the mechanical properties of such hardened steels are closely linked to the morphology and substructure of the martensite.

A typical substructure of lath martensite would consist of blocks and packets. A block is composed of laths that are identically oriented in space, while a packet is a group of blocks that share the same austenite (111) close packed (CP) plane, to which the corresponding (011) martensite plane is almost parallel. The laths within a packet have habit planes that make small angles with respect to each other, but have different crystallographic orientations, while the laths within the blocks have similar crystallographic orientations [10,11]. On the other hand, and from a crystallographic aspect, 24 variants (V1, V2…. V24) divided in 04 CP groups can be present if the transformation follows a K-S OR. These variants will form in pairs of high-angle grain boundaries (HAGBs) and low-angle grain boundaries (LAGBs) to accommodate the strain introduced by the diffusionless martensitic transformation. Variant selection frequently takes place, despite the theoretical possibility of 24 variants existing within a single PAG. Morito et al. [14] reported that the prior austenite grain size (PAGS) has a pronounced effect on the variant selection and substructure formation in low-carbon steels. The smaller the PAGS, the smaller the block size, and the higher the tendency for variant selection. Wang et al. [15] stipulated that a smaller PAGS increases the driving force for lath nucleation and inhibits the formation of multiple variants. Other studies [12,13,16] reported that carbon content in solid solution is one of the main impacting factors for variant selection during martensitic transformation. The higher the carbon content, the lower the selectivity and the higher is the fraction of HAGBs pairs formation.

It has also been reported that the increase in the fraction of HAGBs could result in superior levels of toughness, since the crack propagation is better hindered. Wu et al. [17] reported that the toughness of a high strength steel is improved by the regulation of variant pairs. A higher fraction of HAGBs V1/V2 pairs was accompanied by an increase in the impact toughness. Wang et al. [18] established a correlation between block width and the impact toughness. They found that large blocks led to lower impact toughness values.

In addition to the influence of the HAGB fraction on toughness, it has been reported that $M_{23}C_6$ tempering carbides play a crucial role in controlling both the toughness [19] and the wear behavior [20] of martensitic steels. Specifically, Kipelova et al. [21] found that $M_{23}C_6$ carbides precipitate during the isothermal tempering process, and their formation respects certain ORs with the matrix. It has also been reported that the morphology and distribution of $M_{23}C_6$ carbides are strongly influenced by the underlying martensite substructure [22]. As tempering progresses, these carbides tend to nucleate and grow preferentially along martensite lath boundaries [23], prior austenite grain boundaries (PAGBs) [24], and coincident site lattice (CSL) boundaries, which are high-energy interfaces within the martensitic matrix [25,26]. The size, shape, and spatial arrangement of the $M_{23}C_6$ carbides are directly related to the characteristics of the martensite, including lath width and dislocation density. For example, Sun et al. [27] found that a finer martensite substructure after quenching improves the distribution of carbides through the matrix and a higher carbon content in solid solution promotes the precipitation of spherical shape carbides during tempering.

The control of the PAGS and alloying content in austenite solid solution has been traditionally achieved through thermal routes by adjusting austenitization parameters in conventional quenching and tempering heat treatments. However, while high austenitization temperatures are necessary to fully dissolve alloying elements into the matrix, these elevated temperatures can trigger undesirable abnormal grain growth. To address this issue, innovative heat treatment techniques have recently emerged. Among these, thermal cycling has shown remarkable effectiveness in refining the microstructure without compromising alloy dissolution [28]. Grange [29] was among the first to document that, multiple austenitization cycles could lead to finer microstructures due to the different starting phases having varying phase saturations.

The application of double austenitization (DA) treatment has been reported to be beneficial for most martensitic steels including tool steels. A favorable balance of strength and toughness has been achieved through the application of DA, resulting in overall reductions in both PAGS and carbide size [30,31,32]. Salunkhe et al. [33] examined the effect of DA on D2 tool steel, the study showed that the process yielded to a finer microstructure and enhanced strength. Liu et al. [34] investigated the effect of DA followed by tempering process on the microstructure and mechanical properties of a low carbon 5Cr steel. Their findings revealed that the yield strength showed a modest increase of about 4 %, while the impact toughness was improved more than 40 % due to the refinement of PAGS and martensite block size alongside carbide precipitation. They also noticed that the precipitate size at PAGBs was reduced due to the redistribution of the alloying elements in the matrix. In our recent study on modified AISI A8 steel [35], we demonstrated that DA could improve tool life by up to 130 %. This significant enhancement was attributed to a finer martensitic microstructure, smaller and finer $M_{23}C_6$ carbide dispersion. However, in contrast, Ogel [36] observed a decrease in the intensity factor over multiple austenitization cycles in M2 tool steel, despite PAGS and carbide refinements. They interpreted their findings in terms of the reduced spacing between fine carbides which impeded the movement of the dislocations, thereby diminishing the capacity to absorb shocks. Ali et al. [37] also investigated the effect of DA and tempering on two ultrahigh strength steels and found that unlike other research, the PAGS and block size were increased because of DA. Nonetheless, the impact toughness was improved, with minor decrease of the strength, and this was attributed to the increase in volume fraction of retained austenite (γ_r).

The variability on possible beneficial effects of DA in improving the mechanical properties of highly alloyed tool steels highlights the need for a more fundamental investigation into the mechanisms underlying DA's effects. While DA has been primarily associated with grain refinement, its impact on microstructure and mechanical properties appears to be alloy dependent. Previous research has largely focused on the effects of DA on PAGS and carbide size refinements. However, there is a notable gap in understanding how DA influences martensite substructure formation (blocks and packets) after quenching and the kinetics of alloy carbide precipitation during tempering. Moreover, the mechanisms driving precipitate refinement following DA treatments need to be better understood.

In light of these knowledge gaps, the present study aims to conduct a comprehensive investigation into the impact of double austenitization and tempering treatment on microstructural features and mechanical properties of an AISI A8 cold work tool steel and discuss the underlying mechanisms.

2. Materials and methods

2.1. Heat treatment

The steel used in this study is a modified A8 air-hardening, cold work tool steel, featuring a higher chromium content (8 %. wt) compared to the standard A8 (5 % wt). The full chemical composition was obtained using a SPECTROMAXx arc/spark optical emission spectrometer and is presented in Table 1. The as-received steel was in the annealed state, consisting of a ferritic matrix with annealing $M_{23}C_6$ carbides. Fig. 1.a shows the equilibrium phase diagram, calculated using FactSage [38] and the FS Steel databases, with an enlarged view highlighting the temperatures chosen for this study.

Table 1
Chemical composition of the modified A8 tool steel.

Element	C	Si	Cr	Mn	Mo	Ni	P	S	Fe
Wt %	0.40	0.80	8.00	0.40	1.20	0.14	0.00094	<0.00020	Bal.

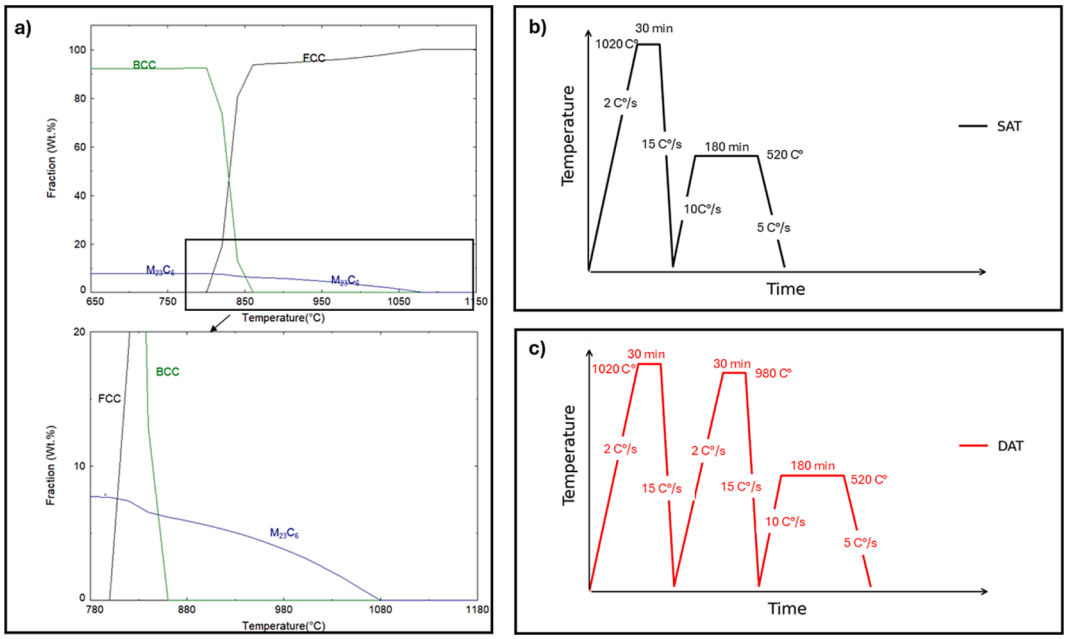

Fig. 1. Heat treatment cycle and parameters: (a) Phase equilibrium simulation of the A8-modified on FactSage, (b) SAT heat treatment, (c) DAT heat treatment.

Two heat treatment protocols were investigated: 1) Single Austenitization Tempering (SAT), the conventional approach for tool steels, comprising one austenitization cycle followed by tempering; and 2) Double Austenitization Tempering (DAT), a novel treatment consisting of two sequential austenitization-quenching cycles, followed by tempering, as illustrated in Fig. 1.b and Fig. 1.c. The HT parameters were chosen based on the thermodynamic simulation and preliminary dilatometry test results. The temperature for the first austenitization in the DAT process (1020 °C) has been carefully selected based on FactSage calculations, which indicate that at this temperature, approximately 4 wt% of carbides remain undissolved. This precise temperature choice is crucial to ensure that carbide dissolution remains incomplete. The undissolved carbides are essential for the subsequent austenitization at 980 °C, where they serve as nucleation sites and act as pinning points to restrict the growth of newly formed austenite grains [33].

Heat treatments were performed using a DIL 805A/D-TA high-resolution dilatometer, allowing precise control of heating and cooling rates crucial for studying phase transformations. Dilatometry samples (⌀ 04 mm × 10 mm cylinders) were prepared parallel to the rolling direction using electrical discharge machining (EDM). SAT samples were heated to 1020 °C for 30 min, while DAT samples underwent an additional austenitization cycle at 980 °C for 30 min. All samples were quenched at a rate of 15 °C/s.

Quenched samples for both conditions were tempered at 520 °C for 180 min (3 h). A heating rate of 10 °C/s was employed to reach the tempering temperature, minimizing transient carbide precipitation during heating. The post-tempering cooling rate was set at 5 °C/s. It must be noted that, while multiple tempering cycles are common in tool steel processing, to address γ_r decomposition and fresh martensite formation [2], this study, focused on a single tempering cycle to isolate the effects of the DA process on carbide precipitation.

2.2. Microstructure characterization

For as-quenched samples, thermal etching (TE) [39] was employed to reveal both PAGs structure and martensite morphology, overcoming the limitations of conventional chemical etching that proved to be insufficient, revealing only the PAGBs. Thermally etched samples were observed using backscattered electron (BSE) imaging.

Sample preparation involved precise sectioning in the longitudinal-central direction, followed by mechanical polishing until P4000 grit followed by a final polishing step using a diamond suspension powder (⌀1μm). For advanced EBSD analysis, an additional surface preparation step was introduced: vibratory polishing for 1 h with a silica powder (⌀ 0.5 μm) followed by Hitachi-IM4000 PLUS ion milling for 25 min. This systematic sample preparation ensured the removal of all deformation bands, critical for high-quality EBSD data acquisition.

The EBSD maps were strategically acquired from regions exhibiting a range of grain sizes, ensuring a diverse sampling of the microstructure. This approach allowed for a detailed analysis of how grain size variations influence martensite substructure formation. EBSD mapping was performed using a Hitachi SU-8230 field emission scanning electron microscope (FE-SEM). To quantitatively assess the effect of PAGS on martensite substructure formation, crystallographic and texture analysis were conducted. This involved post-processing of EBSD data from six distinct grains using MATLAB with the MTEX library [40], providing a statistically significant dataset for microstructural characterization.

For quenched and tempered samples, the preparation protocol mirrored that of the as-quenched samples, with the addition of 3 % Nital etching to reveal tempered microstructural features. Phase identification and quantification were carried out using X-ray diffraction (XRD) on an X'Pert Panalytical diffractometer equipped with Co Kα radiation. The XRD analysis was optimized with an acceleration voltage of 45 kV and a 2θ scan range from 20° to 145°, using a step size of 0.05° to ensure high-resolution diffraction patterns. The resulting data were analyzed

using HighScore software. In addition, fraction and morphology of secondary carbide particles were analyzed by SEM.

2.3. Thermal analysis during tempering

Thermal analysis (TA) was conducted to study the kinetics of carbide precipitation during tempering in the dilatometer. The linear dilatation was measured using a linear variable displacement transducer (LVDT) with a resolution of $\Delta L/^{\circ}C = 0.05\ \mu m/0.05\ ^{\circ}C$. A K-type thermocouple was spot-welded to the center of the sample's surface. The relative change in length (RCL) was recorded during the isothermal hold at 520 °C. The dilatometer was equipped with a fused silica push rod, selected for its extremely low coefficient of thermal expansion (approximately 0.5×10^{-6} /°C [41]). For the 3-hour isothermal experiments at 520 °C, the expansion of the push rod was negligible and did not affect the accuracy of the dimensional change measurements.

The evaluation of kinetic parameters, such as the activation energy, could be done by studying the evolution of a physical property, denoted as p, over the transformation. In this study, the TA helped in monitoring the precipitation of alloy carbides where the physical property under consideration was the RCL. The fraction of the newly formed phase, denoted as f, can be expressed as follows [42]:

$$f = \frac{p - p_{min}}{p_{max} - p_{min}} \tag{1}$$

here p represents the length of the sample at time t, while p_{max} and p_{min} are the maximum and minimum length of the sample (before and after the transformation), respectively. In isothermal conditions, a typical heterogenous transformation can be described by the Johnson-Mehl-Avrami-Kolmogrov (JMAK) equation [43]:

$$f = 1 - \exp(-\beta^n) \tag{2}$$

with:

$$\beta = k(T)t = k_0.\exp\left(-\frac{Q}{R.T}\right).t \tag{3}$$

where n and k_o are the Avrami constant coefficients, T the temperature (Kelvin), Q the activation energy (kJ/mole), t the time(seconds) and R the gas constant (8.31 J/mole).

To determine the activation energy Q, tempering temperatures were varied in the range of 480–520 °C.

2.4. Mechanical tests

Mechanical property tests were conducted with at least three samples per test and condition. Toughness evaluation was performed using Charpy-V notch (CVN) specimen (55 mm × 10 mm × 10 mm) as described in ASTM E23 standard [44] at room temperature, where a hammer impacts the opposite surface of the notch.

ASTM G65 procedure B standard [45] was selected because it simulates the type of abrasive wear encountered in many practical applications of modified A8 steel, particularly in wood cutting industries where sand and other hard particles are present. In such environments, components are subjected to dry, high-stress, three-body abrasion similar to the conditions replicated by the ASTM G65 rubber wheel test. In this procedure, a rectangular specimen (25 mm × 76 mm × 12.7 mm) is exposed to abrasive sand for 10 min under a normal load of 130 N. The test employs a rotating rubber wheel, with a total of 2000 revolutions during the test duration. The lineal abrasion distance for Procedure B is 1436 m. The wear rate is calculated using the following formula:

$$Wearrate = \frac{Massloss(mg)}{LinealAbrasion(m)} \tag{4}$$

The mass loss is determined by measuring the mass of the specimen before and after the test.

Both Charpy impact test and wear specimens underwent heat treatment in a vacuum furnace using the same thermal cycle used in the dilatometer. A thermocouple was attached to a piece adjacent to the specimens for temperature control during the heat treatments in the vacuum furnace.

Hardness measurements were performed using a Struers Duramin-40 Vickers microhardness tester with a 10 kg load and a 10-second dwell time. For each specimen, at least 10 indentations were made, and the average Vickers hardness value was revalued to the Rockwell C scale (HRC) for easier comparison.

3. Results

3.1. Microstructure characteristics of the as-quenched sample

3.1.1. Lath martensite microstructure

The morphologies of the PAG in the as-quenched SAT and DAT samples are presented in Fig. 2. Both samples exhibit a lath martensite microstructure, with PAGs subdivided into packets. Thermal etching was employed to reveal the boundaries, proving particularly effective in delineating the PAGBs in the SAT samples (Fig. 2.a). However, this technique presented challenges in the DAT samples (Fig. 2.b), as the boundaries of newly formed grains after the second quenching potentially interfered with those formed during the first quenching [39]. Notably, the DAT treatment appears to have significantly reduced the PAGS compared to the SAT treatment. This observation is consistent with our previous findings on the same steel, where detailed analysis showed that the DAT process effectively refines the PAGS [35].

Interestingly, despite being austenitized at a higher temperature (1020 °C), the SAT samples exhibit a higher proportion of undissolved carbides compared to the DAT ones. This observation is particularly interesting given that higher austenitization temperatures typically promote greater carbide dissolution. The presence of these undissolved carbides in the SAT samples may be attributed to insufficient time for complete dissolution at the single austenitization temperature. In contrast, the DAT process, with its two-stage austenitization, appears to have facilitated more complete carbide dissolution, potentially due to the cumulative time at elevated temperatures. It should be noted that the identification and comparison of undissolved carbides in this section are based on visible features in SEM images. EBSD analysis was employed to characterize the morphological changes and sub-structure of the martensite. Fig. 3.a and Fig. 3.b present the image quality (IQ) maps for the SAT and DAT conditions, respectively, which delineate the lath martensitic microstructure. Fig. 3.c and Fig. 3.d present the EBSD phase maps for both conditions, highlighting the distribution of martensite (α') and γ_r. Due to the very low fraction of undissolved carbides, these were not indexed in the EBSD analysis. It should be noted that γ_r appears mainly as blocky regions, although the blocks are very small. In some areas, thin film-like γ_r are also observed. The measured γ_r fraction is approximately 6 % for SAT and 8 % for DAT, with an estimated uncertainty of ±1 % for both conditions. The corresponding reconstructed PAGs are shown in Fig. 3.e and Fig. 3.f. The reconstruction of PAGs was performed using inverse pole figures (IPFs) of indivdual lath martensite variants employing the new variant vote approach, recently developed on MTEX [46,47].

For detailed martensite variant analysis, six representative grains were selected from the EBSD maps, as shown in Fig. 3.g and Fig. 3.h. The selection criteria were as follows: the two largest grains (PAGS > 20 μm) in each map (G1 for SAT and G4 for DAT), two grains of comparable intermediate (20 μm > PAGS > 10 μm) size (G2 for SAT and G5 for DAT), and two small (10 μm > PAGS) grains (G3 in red for SAT and G6 in brown for DAT, indicated by black arrows). This selection ensured a comprehensive analysis covering various grain sizes.

3.1.2. Effect of PAGS on martensite variant pairing and variant selection

Based on the calculated near K-S OR (which deviated by 0.44° from

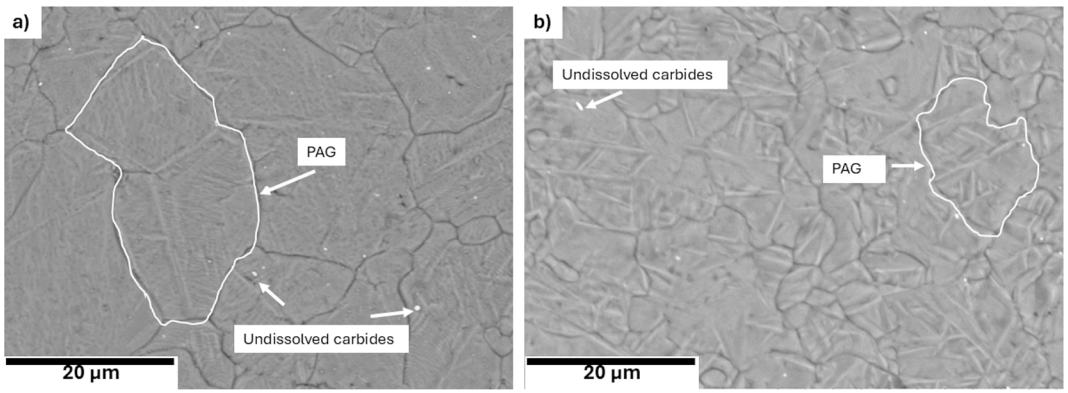

Fig. 2. BSE-SEM micrographs showing grooves formed by thermal etching. PAGs and undissolved carbides are highlighted. (a) SAT sample. (b) DAT sample.

the ideal OR) using the library OR tools [47], the 24 possible martensite variants were computed and divided, based on the classification method, into 03 Bain groups and 04 Close Packed (CP) planes consisting each of 06 variants (e.g., V1-V6 for CP1) (CP1: (111)γ//(011)α, CP2: (1–11)γ//(011)α, CP3: (−111)γ// (011)α and CP4: (11–1)γ//(011)α) [11]. Theoretically, in a completely isotropic material, these variants should have equal probability of formation. However, due to texture inherited from prior processing and the material's thermomechanical history, variant probabilities often deviate from this ideal distribution.

Table 2 shows the calculated 5 variants of the same CP group with respect to V1, computed using MATLAB for the investigated steel. From a crystallographic perspective, variants V3 and V5 are equivalent. The analysis reveals that pairs V1/V2 could form twin-related boundaries, V1/V3(V5) and V1/V6 are HAGBs, while V1/V4 is a LAGB.

Fig. 4 presents a detailed variant pairing analysis that highlights the differences between the SAT and DAT samples. The analysis was conducted by projecting the three other CP groups (CP2, CP3, CP4) onto CP1, allowing for a comparative analysis of variant pairing across all crystallographic packets. In the SAT treatment, the distribution of variant pairs is as follows: 28 % for twin-related V1/V2 boundaries, 19 % for HAGBs V1/V3(V5), 43 % for LAGBs V1/V4, and 10 % for HAGBs V1/V6. In contrast, the DAT treatment shows an increase in twin-related boundaries to 30 %, and HAGBs V1/V3(V5) rise to 22 %, while the fraction of LAGBs V1/V4 decreases to 36 %.

Fig. 5 presents the variant analysis for the six selected grains (G1-G6) from both SAT and DAT samples. It is important to note that a K-S variant represents a group of laths, with laths being considered the smallest sub-unit in martensite, characterized by small misorientations within the variant.

In the largest grains (PAGS > 20 µm), G1 (SAT) and G4 (DAT), all 24 possible K-S variants are observed, indicating a high degree of transformation freedom. However, a notable difference in the lath martensite morphology is evident.

In G1, two distinct morphologies can be identified:

- Large regions (e.g., V15, V21) that could be classified as 'coarse variants,' which make direct contact with the PAGBs, their substantial size suggests they formed early in the transformation process, potentially nucleating at the PAGBs and growing inward [48]. These coarse regions may result from lower nucleation rates.
- Smaller regions of finer variants: These are generally trapped between the large K-S variants. Their formation might be a consequence of the remaining austenite transforming under more constrained conditions, leading to a refinement in lath size.

In contrast, G4 presents a different structure:

- Fine, elongated plate-like variants: These dominate the G4 grain, suggesting a more uniform nucleation and growth process.
- Smaller and finer variants: These are interspersed between the elongated plates, filling the interstitial spaces. Their presence indicates a highly efficient use of the available volume for transformation, possibly due to increased nucleation sites or a more controlled growth.

For the medium-sized grains (20 µm > PAGS > 10 µm), G2 (SAT) and G5 (DAT), a slight reduction in variant diversity is observed, particularly in G2. In contrast, G5 maintains a relatively high variant diversity, indicating that the DAT treatment preserves transformation flexibility even as grain size decreases. The smallest grains (10 µm > PAGS), G3 (SAT) and G6 (DAT), show the most noticeable difference. G3 exhibits a highly pronounced variant selection, with only a few variants from a single CP group (CP2) appearing to have nucleated. This severe variant selection in small SAT grains could lead to anisotropic properties at the microscale. Conversely, G6 maintains a surprisingly high variant diversity despite its small size, showcasing multivariant formation from all possible CP groups. This suggests that the DAT treatment effectively mitigates the variant selection typically observed in smaller grains, potentially leading to more isotropic properties even at fine scales.

Figs. 6 and 7 illustrate the distribution of CP and Bain groups, respectively, across the six selected grains (G1-G6) from both SAT and DAT samples. The area occupied by each CP and Bain group reveals the dominant transformation paths in each grain and are presented in Table 3. As it can be seen, in the largest SAT grain, G1, the CP groups show a relatively balanced distribution (18.4 % CP1, 24.7 % CP2, 29.5 % CP3, 27.4 % CP4), while the Bain groups are also evenly distributed (33.9 % B1, 35.3 % B2, 30.8 % B3). This suggests that no single transformation path dominates in large SAT grains. In contrast, the largest DAT grain, G4, shows a slight preference for CP1 and CP2 (27.9 % and 31.5 % respectively) with an almost perfectly balanced Bain group distribution (33.8 % B1, 32.9 % B2, 33.3 % B3), indicating that the DAT treatment promotes a more uniform transformation across all possible orientations.

For the medium-sized grains, G2 (SAT) shows a preference for CP2 (30 %) and a strong dominance of Bain1 (44.4 %), suggesting a more selective transformation path. G5 (DAT), however, maintains a more balanced distribution in both CP and Bain groups, with a slight preference for CP2 (40 %) and Bain2 (38.6 %). It is interesting to note that, here again, the most observed difference is seen in the smallest grains. G3 (SAT) shows extreme selectivity with CP2 dominating at 75.8 %, while the Bain groups remain surprisingly balanced (36.7 % B1, 32.8 % B2, 30.5 % B3). This suggests that in small SAT grains, the transformation is heavily influenced by the CP plane orientation but maintains diversity in the Bain distortion. Conversely, G6 (DAT) maintains diversity in both CP and Bain groups, with a slight preference for CP1 (33.2 %) and relatively balanced Bain groups (34.7 % B1, 31.1 % B2, 34.2 % B3).

In summary, the variant analysis shows the dispersion of the CP and

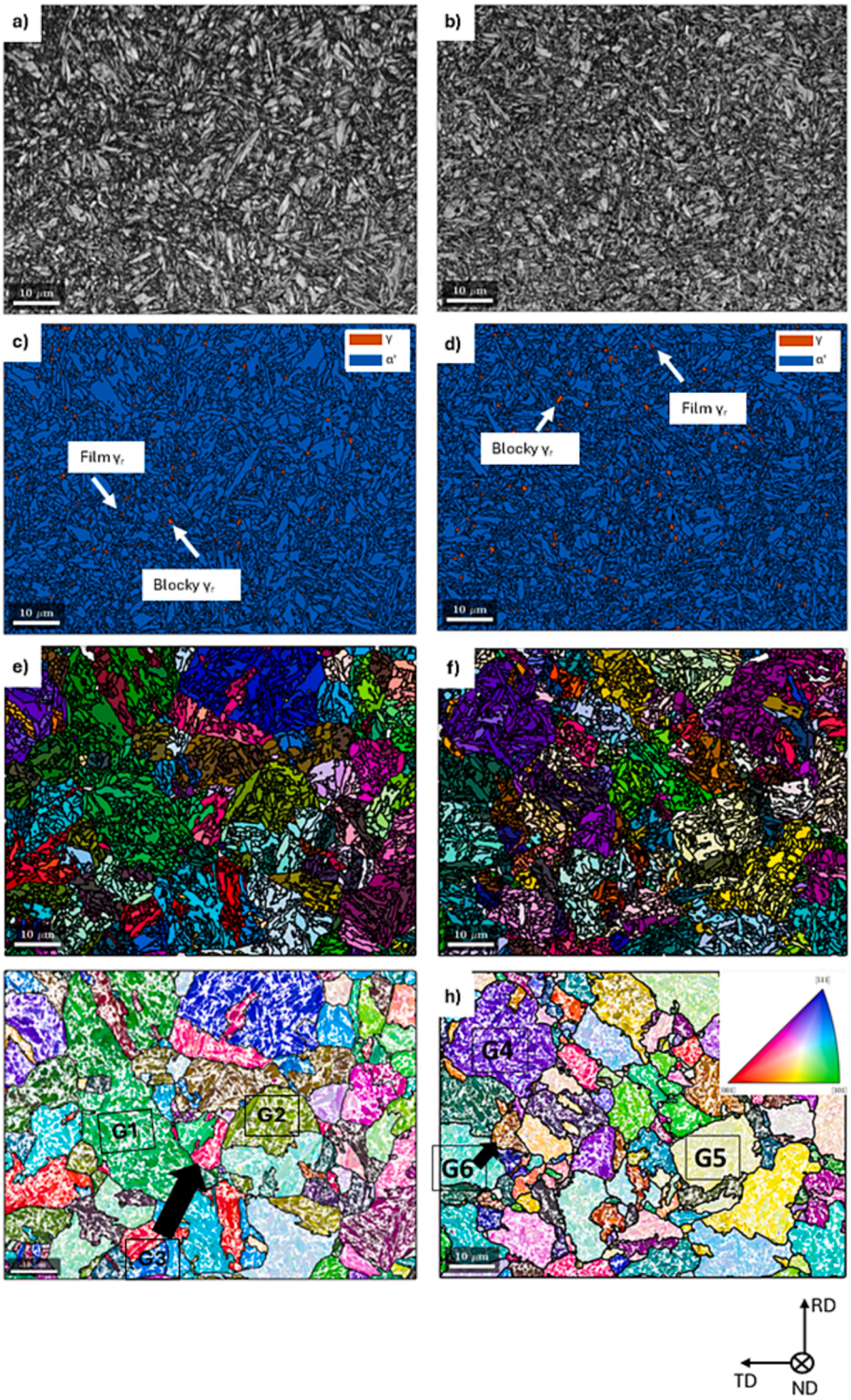

Fig. 3. EBSD characterization of quenched microstructure. Image quality for (a) SAT and (b) DAT. Phase maps showing martensite and retained austenite (γ_r) for (c) SAT and (d) DAT. Grouped variants for (d) SAT and (f) DAT. PAG reconstruction showing the selected grains for variants analysis, (g) SAT and (h) DAT.

Table 2
The 6 variants of CP1 and the corresponding misorientation angles in respect to V1 for modified A8 steel.

Variant	Angle	Rotation axis	Variant	Angle	Rotation axis
V1	0°	[0.0000, −0.0000,0.3489]	V4	5.87°	[0.0239, −0.0000,0.3481]
V2	60.34°	[0.1789,0.1883,0.2330]	V5	57.10°	[0.1760,0.1649,0.2521]
V3	57.10°	[0.1649,0.1760,0.2521]	V6	56.16°	[0.2463,0.0215,0.2463]

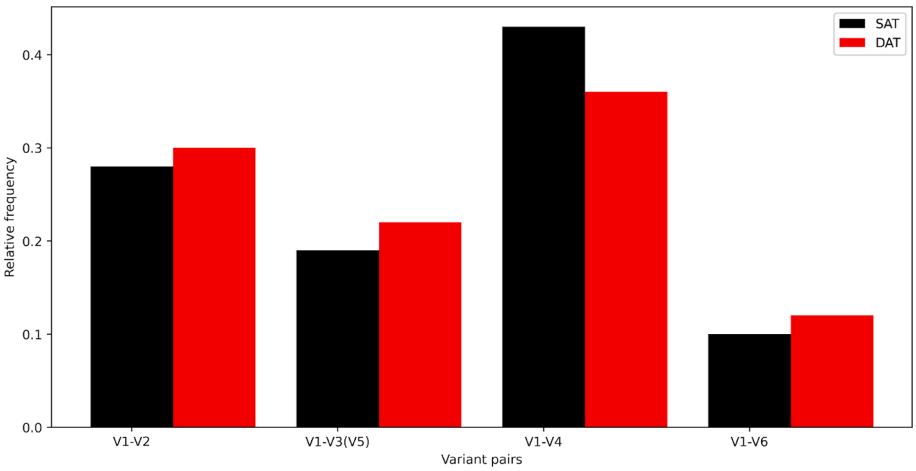

Fig. 4. EBSD characterization of quenched microstructure. Variant pairs frequency area distribution. SAT in black and DAT in red. (For interpretation of the references to color in this figure legend, the reader is referred to the web version of this article.)

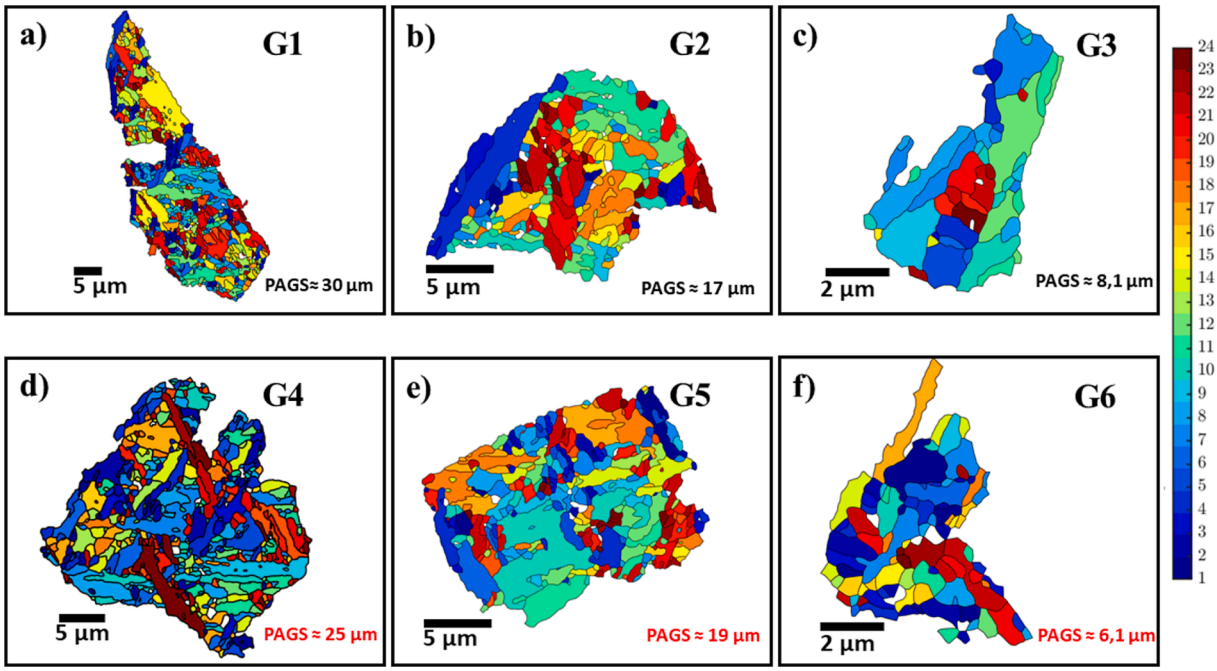

Fig. 5. EBSD characterization of quenched microstructure for the reconstructed prior austenite grains showing the possible 24 variants. SAT (G1, G2, G3) (a-c), and DAT (G4, G5, G6) (d-f).

Bain groups within the PAGs. It is clearly distinguishable that DAT results in a smaller packet size, as compared to SAT samples. Moreover, in any given reconstructed PAG, the probability of finding more than one packet is higher in DAT samples, whereas some reconstructed PAGs in the SAT show an exclusive CP group with less-pronounced sub-block formation. Also, this variant selection trend is more effective in smaller PAGs in SAT samples but seems to be insensitive to the PAGS in the DAT samples. The importance of having possibly 6 variants within one CP group has been studied by Morito et al. [11] who found that the combination of possible 6 variants drastically reduces the shape strain from 0.242 for a single variant to 0.024 for a combination of 6 variants in one CP group.

3.1.3. *Effect of PAGS on martensite block width*

To quantitatively assess the impact of PAGS reduction on martensite substructure formation, a detailed analysis of the martensite block width was conducted. Fig. 8 illustrates the block width distribution for the six selected grains. The block width was calculated by projecting all boundary points onto the vector perpendicular to the trace of the (111) plane, as exemplified in Fig. 8.g for grains G2.

In the SAT samples, a tendency for block width to increase with increasing PAGS was observed. As PAGS decreased from G1 to G3, the average block width correspondingly reduced from 0.38 µm to 0.35 µm. Surprisingly, this trend was not replicated in the DAT samples. Despite the PAGS decrease from G4 to G6, the mean block width remained relatively constant at approximately 0.32 µm. To further investigate this phenomenon, the analysis was extended to include 14 additional grains (7 for SAT and 7 for DAT) with PAGS ranging from 5 µm to 30 µm. The PAGS was estimated by measuring the mean grain diameter of the 2D section for each grain. The results of this expanded analysis are presented in Fig. 9.

As it can be seen, for the SAT samples, the linear relationship between PAGS and block width is largely maintained particularly for grains ranging from 3 µm to 15 µm. In this range, a positive correlation

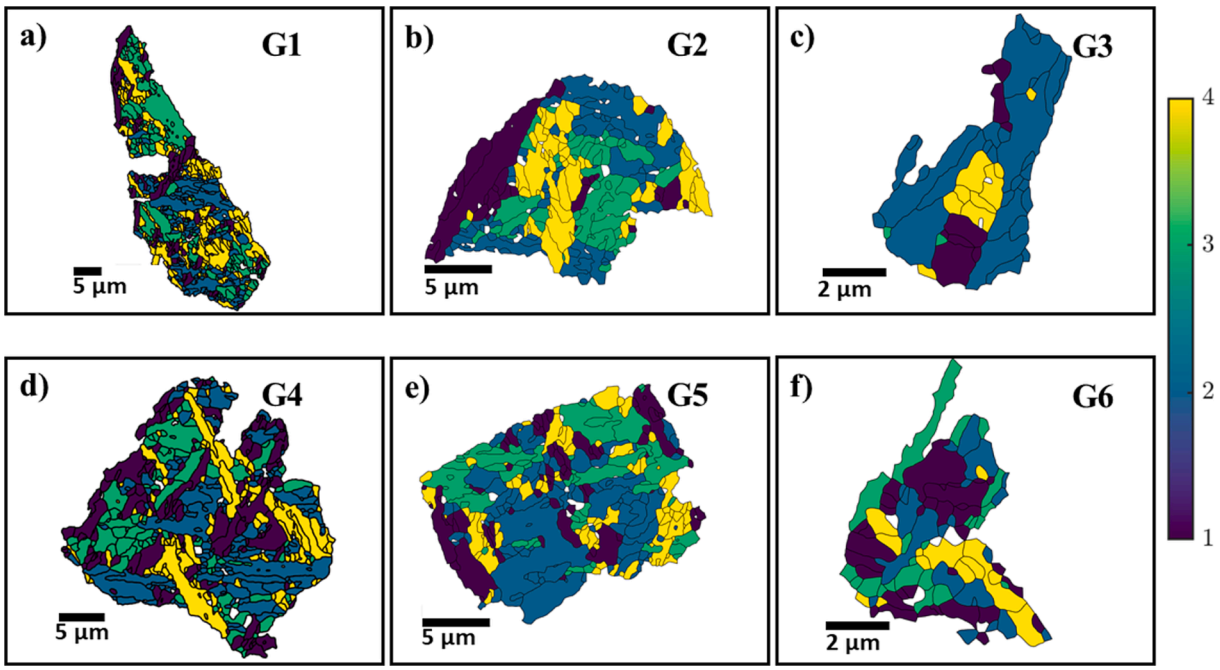

Fig. 6. EBSD characterization of quenched microstructure for the reconstructed prior austenite grains showing the possible 04 packet groups. SAT (G1, G2, G3) (a-c), and DAT (G4, G5, G6) (d-f).

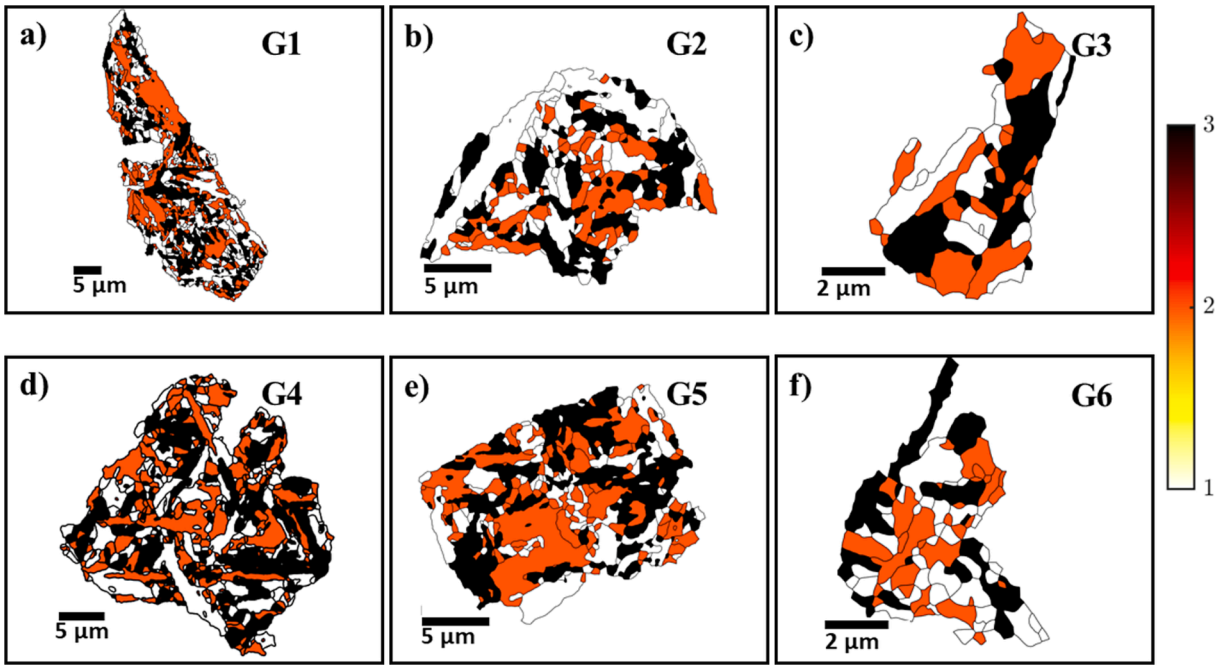

Fig. 7. EBSD characterization of quenched microstructure for the reconstructed prior austenite grains showing the possible 03 Bain groups. SAT (G1, G2, G3) (a-c), and DAT (G4, G5, G6) (d-f).

seems to exist. An increase in PAGS from 3 µm to 15 µm correspond to an increase in block width from 0.34 µm to 0.47 µm. Interestingly, for PAGS beyond 15 µm, up to 30 µm (G1), a negative slope is observed, resulting in a decrease in block width.

In contrast, the DAT samples exhibit a markedly different behavior. Despite PAGS variations from 4 µm to 25 µm (G4), the block width does not show the ascending trend observed in the SAT samples. Instead, it fluctuates around a mean value of 0.32 µm, regardless of the increase in PAGS. In the DAT samples a very weak dependence of block width on PAGS is observed. This distinct behavior in DAT samples might be attributed to the substructure formation discussed in section 3.1.2, which could potentially influence the relationship between PAGS and block width in these samples.

3.2. Microstructure characteristics of tempered samples

3.2.1. Microstructure characteristics of carbides

Fig. 10 displays the microstructures of the SAT and DAT conditions after tempering. In both cases, the microstructure is composed of tempered martensite and carbides. The observation that a significant

Table 3
Dispersion of CP groups and Bain groups for the six grains (G1-G6).

Grain	Weighted Area CP groups				Weighted area Bain groups		
	CP1	CP2	CP3	CP4	B1	B2	B3
G1	18,4 %	24,7 %	29,5 %	27,4 %	33,9 %	35,3 %	30,8%
G2	22,4 %	30 %	22,7 %	24,9 %	44,4 %	23,9 %	31,7 %
G3	12,8 %	75,8 %	0,5 %	10,9 %	36,7 %	32,8 %	30,5 %
G4	27,9 %	31,5 %	19,9 %	20,7 %	33,8 %	32,9 %	33,3 %
G5	19,7 %	40 %	23,5 %	16,8 %	25,9 %	38,6 %	35,5%
G6	33,2 %	24 %	24,9 %	17,9 %	34,7 %	31,1 %	34,2 %

fraction of these carbides appears only after tempering indicates that their precipitation is predominantly induced during this heat treatment step. For clarity, these precipitates will be referred to as secondary carbides throughout the manuscript.

Examining the carbides in detail, three main morphologies can be identified: large secondary carbides (LSCs), elongated secondary carbides (ESCs), and small secondary carbides (SSCs). In this study, the particles have been classified according to their size and shape: SSCs are defined as carbides with a size <0.5 μm, LSCs as those with a size >0.5 μm, and ESCs as carbides with an aspect ratio (c/a) >2. In the SAT conditions, both LSCs and ESCs are present. The LSCs generally exhibit a globular shape, while the ESCs are characterized by a higher aspect ratio (c/a) and are primarily located along PAGBs. Notably, within both SAT and DAT conditions, LSCs can be further classified based on their location: those situated at PAGBs, often displaying at least a coherent interface with one of the adjacent grains, and those located entirely within the grains. In contrast, the DAT sample shows a quasi-absence of ESCs. The LSCs present seems to be more spherical, and they are accompanied by SSCs. The dispersion of carbides in DAT conditions appears more homogeneously distributed.

Quantitative analysis is presented in Table 4 further highlights these differences. In the SAT condition, ESCs account for 3.2 ± 0.9 %, LSCs for 5.7 ± 1.5 %, and SSCs for 1.3 ± 0.4 %. In contrast, the DAT condition exhibits a markedly lower fraction of ESCs (< 0.5 %), a slightly reduced LSC fraction (5.2 ± 1.6 %), and a noticeably higher content of SSCs (2.5 ± 1 %). These results indicate that the DAT process not only suppresses the formation of elongated secondary carbides but also promotes a finer and more homogeneous distribution of carbides, as evidenced by the increased fraction of SSCs.

Microstructures close to those observed here have been reported in D2 tool steel. However, D2 typically contains both primary carbides and secondary carbides. In our steel, most carbides were dissolved during austenitization, resulting in the absence of primary carbides. Instead, only secondary carbides precipitated during tempering. Both types of secondary carbides observed in our samples (LSCs and SSCs) have been reported to correspond to $M_{23}C_6$ carbides by Das et al. [49] Interestingly, In sub-zero treated Vanadis 6 tool steel, Jurči et al.[50] observed

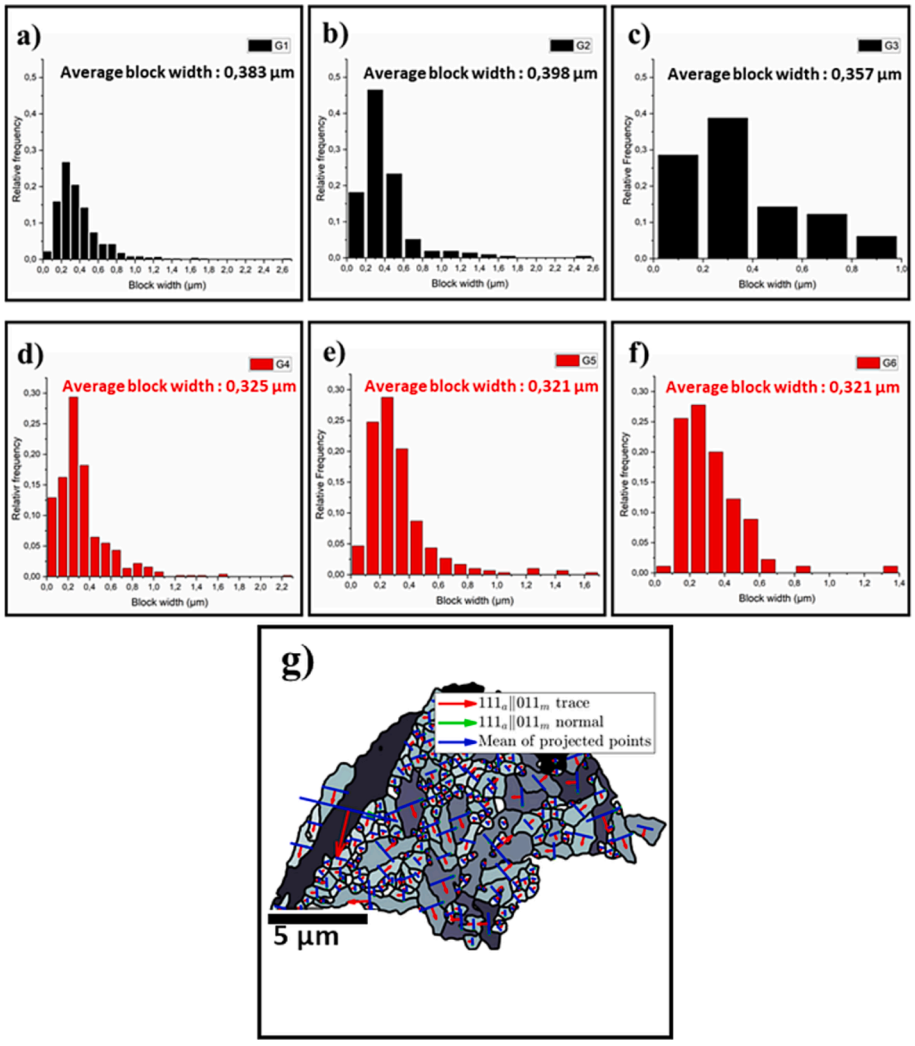

Fig. 8. EBSD characterization of quenched microstructure for the reconstructed prior austenite grains(G1-G6) showing the Block width distribution (a-f). (g) Example of the projection points on G2.

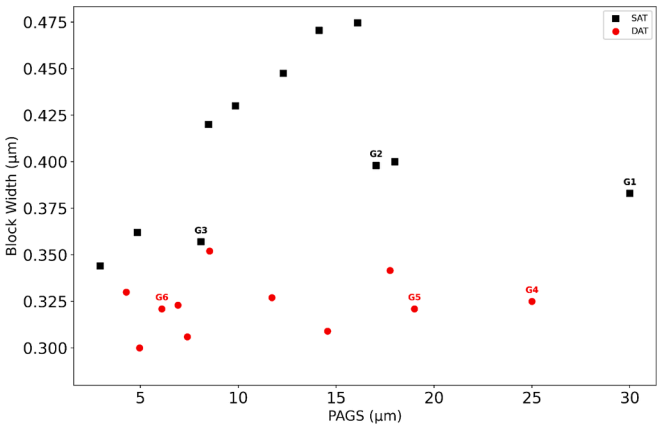

Fig. 9. Evolution of block width as a function the PAGS for 20 studied grains. SAT in dark squares, DAT in red circles. (For interpretation of the references to color in this figure legend, the reader is referred to the web version of this article.)

globular SSCs by transmission electron microscopy (TEM) and they have been identified as orthorhombic M_3C (alloyed cementite) rather than $M_{23}C_6$. Since these carbides were identified even in non-tempered samples, their stability remains uncertain and they may represent a transient or metastable phase.

Beyond the carbides observable by SEM, it is important to recognize that carbides formed during tempering may exist in a variety of forms and sizes, including nanocarbides that are below the resolution limit of SEM. Numerous studies [51,52,53,54] have demonstrated that a significant portion of tempering-induced carbides in tool steels, particularly those responsible for secondary hardening, are nanometric in size. These nanocarbides can play a crucial role in the mechanical properties of tool steels, but require higher-resolution techniques such as TEM for accurate observation and identification. In the present study, our SEM observations were limited to larger secondary carbides.

Turning to our XRD analysis, the patterns revealed the presence of martensite, $M_{23}C_6$ carbides, and a weak (111) γ_r peak in the SAT condition as shown in Fig. 11. This indicates that the DAT treatment does not alter the composition of the precipitates, which remain $M_{23}C_6$, but primarily affects their morphology. It should be noted that, due to the crystallographic similarities and close lattice parameters and space group, distinguishing between $M_{23}C_6$ and M_6C carbides can be challenging [55]. Nevertheless, Kim et al.[56] studied the evolution of carbides in cold work tool steel and their thermodynamic stability throughout the entire thermal cycle, from casting to tempering. They found that while M_6C carbides may form after annealing, these carbides are completely dissolved in favor of $M_{23}C_6$ during subsequent tempering, indicating their lack of stability in the final microstructure. Therefore, we consider the observed carbides to be predominantly $M_{23}C_6$, most of which precipitated during tempering.

It is also noteworthy that the amount of γ_r after quenching was slightly higher in the DAT sample. However, after tempering, the austenite peak is not detected in the XRD pattern of the DAT sample, whereas a small amount (0.8 %) is still present in the SAT sample. It should be emphasized that the absence of a detectable austenite peak in the DAT condition does not necessarily mean that γ_r is completely absent. Rather, it may indicate that its quantity is below the detection limit of the XRD technique used in this study. However, very small trace amounts of γ_r persist in the DAT sample as seen in Fig. 10.b, but at levels too low to be quantified by XRD.

3.2.2. Phase transformations during tempering

3.2.2.1. Retained austenite decomposition and transient carbide precipitation during heating. The significant differences observed in carbide morphologies suggest that the phase transformation kinetics differ between the two heat treatments. During tempering of martensitic steels containing high carbide-forming elements, four main stages are generally recognized according to Bhadeshia [57], though these stages may overlap depending on the alloy composition and processing conditions. Stage I involves carbon atom redistribution and pre-precipitation processes of some transient carbides, which can begin at very low temperatures, sometimes even at room temperature, as shown by previous studies [58,59]. This is followed by the decomposition of γ_r (stage II), which in alloyed steels typically occurs at high temperatures [60]. Stage III is characterized by the transformation of transition carbides, such as ε-carbide, and cementite [61], which may also form at relatively low temperatures, as shown by Ďurica et al.[54]. Finally, stage IV involves the precipitation of alloy carbides at higher tempering temperatures. It should be noted that the precise temperature ranges and sequence of these transformations can vary, and that the different stages may proceed simultaneously or partially overlap.

The evolution of stages I, II, and III can be effectively studied by analyzing dilatometric curves obtained during non-isothermal heating. Fig. 12 presents the derivative of the RCL with respect to temperature (d$(\Delta L/L_0)$/dT) during continuous heating in the tempering process. Between approximately 120 °C and 200 °C, a slight drop in the derivative curve is observed in the SAT sample. This behavior closely resembles phenomena reported by Pacyna [62], where a contraction in strain prior

Table 4
Quantitative analysis data after tempering treatment.

Phase	SAT	DAT
ESCs	3.2 ± 0.9	<0.5 %
LSCs	5.7 ± 1.5	5.2 ± 1.6
SSCs	1.3 ± 0.4	2.5 ± 1
γ_r	0.8 %± 0.2	<0.5 %

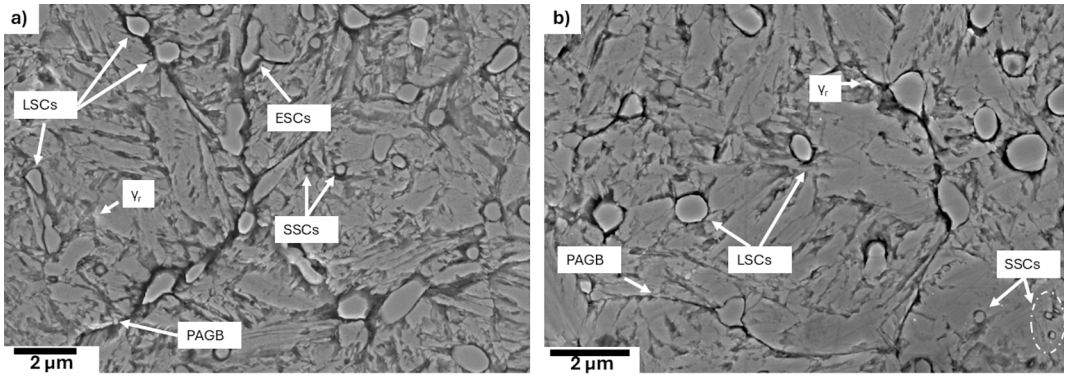

Fig. 10. SE-SEM micrographs showing the different carbide morphologies precipitated during isothermal tempering. (a) SAT, (b) DAT.

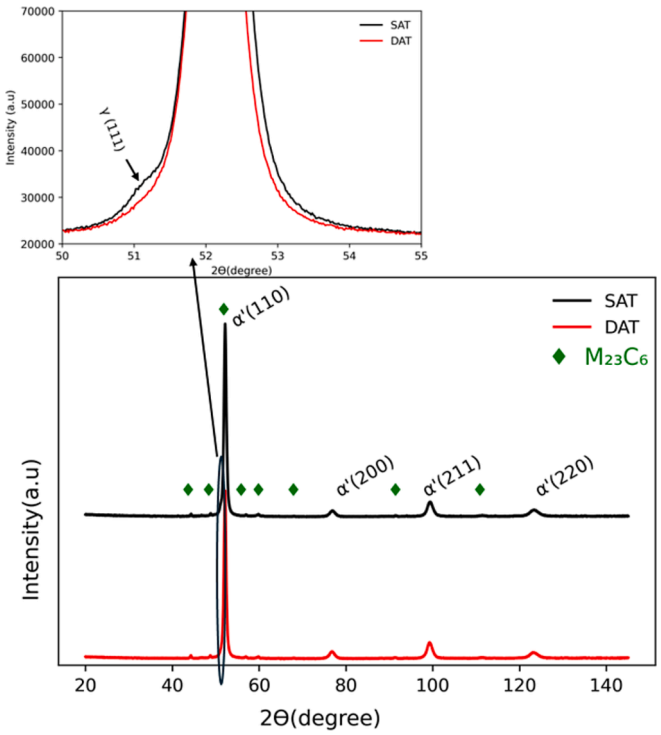

Fig. 11. XRD patterns of the investigated steel quenched and tempered. SAT in dark, DAT in red, $M_{23}C_6$ in green diamonds. The inset provides an enlarged view of the γ_r (111) peak. (For interpretation of the references to color in this figure legend, the reader is referred to the web version of this article.)

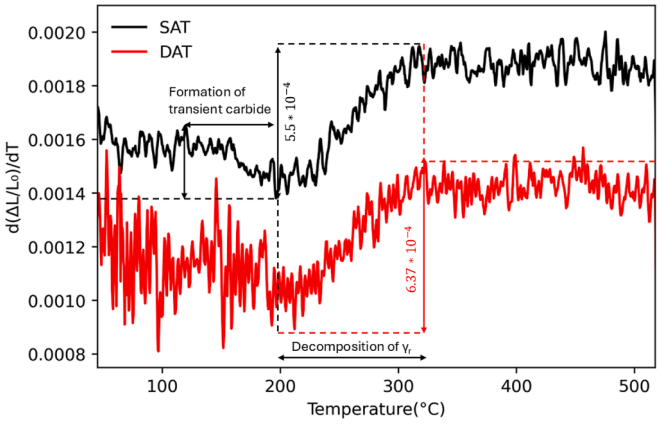

Fig. 12. The derivative length change as a function of the temperature during continuous heating from 20 to 520C.

to the onset of γ_r decomposition has been attributed to the precipitation of transient carbides, primarily ε-carbide. Such carbides are known to form by extracting carbon from supersaturated martensite and typically precipitate at tempering temperatures up to 200 °C as shown by Barrow et al.[63]. In contrast, this contraction is not evident in the DAT samples. Above 200 °C, both SAT and DAT samples exhibit a pronounced increase in the derivative curve, which continues up to around 320 °C. According to Cui et al.[60], this transformation is attributed to the decomposition of γ_r during stage II, likely corresponding to the least stable fraction due to its lower carbon content. It should be noted that despite the similar temperature profiles, a notable difference in intensity is observed between the two conditions. Specifically, the transformation peak in the DAT samples is more pronounced, indicating that a larger fraction of γ_r has already transformed during the heating stage compared to SAT. Following the completion of γ_r decomposition, the derivative curve stabilizes for both samples, indicating the cessation of major phase transformations up to 520 °C.

3.2.2.2. Kinetics analysis of M23C6 carbide precipitation during isothermal tempering. In stage IV of tempering, given sufficient time, non-transformed γ_r could transform into a mixture of ferrite and cementite. If a steel tends to form alloy carbides during isothermal tempering, then the direct decomposition of γ_r will start after the completion of carbide formation. This direct transformation of γ_r is characterized by an expansion in the dilatometric curve [64,65]. Previous studies have shown that the reduction in RCL ($\Delta V/V_0 \approx 3\Delta L/L_0 < 0$) during isothermal holding could be attributed to either alloy carbide precipitation or loss of martensite tetragonality [65]. Since microstructural analysis in this study demonstrated that most carbides precipitated during tempering are $M_{23}C_6$, the observed reduction in RCL can thus be primarily ascribed to the precipitation of these carbides. Therefore, kinetics studies and the determination of activation energy are needed to provide insights into the nature of the transformation. To achieve this, the dilatometric results are converted into kinetic equations.

Fig. 13 presents the evolution of the RCL as a function of time during isothermal tempering at 520 °C. As shown in the Fig. 13, the reduction in RCL for the DAT samples is approximately 30 % smaller than that observed for the SAT samples. This reduced amplitude in RCL suggests a lower extent of phase transformation, which is consistent with data presented in Table 4.

Modeling the kinetics of $M_{23}C_6$ precipitation was done using the JMAK equation [43] and the results of transformed fraction as a function of time are reported in Fig. 14. The results show that the incubation time is longer for DAT compared to SAT which implies a slower nucleation and growth of carbides. The determination of the Avrami parameters n and k_0 was done by plotting ln (ln(1/1-f)) against ln(t) with the exponent n, being the slope of the line, and the constant k_0 calculated from the intercept with y-axis, as shown in Fig. 15.a. The values of n = 1.20 and n = 1.24 for SAT and DAT, respectively suggest that the mechanisms of this heterogeneous phase transformation might be similar. It is worth mentioning that in diffusion-controlled phase transformations, an n value close to 1 would mean that precipitation takes place at grain boundaries and lath boundaries [25].

To further understand the kinetics of the tempering process and its effect on the microstructure, we conducted additional tempering treatments at three different temperatures: 480 °C, 500 °C, and 520 °C. These experiments allowed us to calculate the activation energy for the precipitation process during tempering. By plotting ln(k) versus 1/T, where

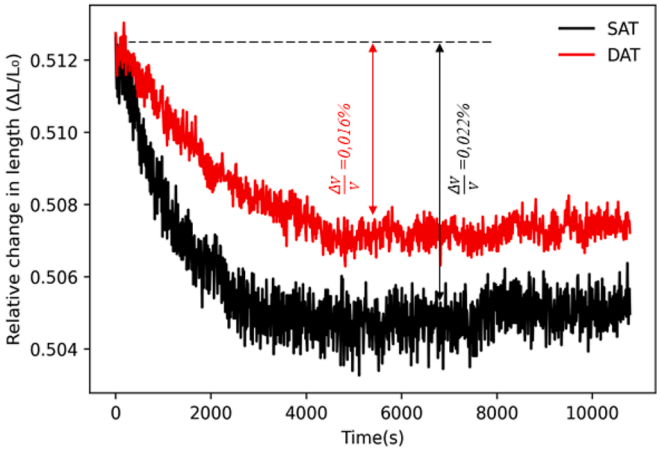

Fig. 13. Relative Change in length during isothermal tempering at 520C showing the contraction of the samples. SAT in black and DAT in red line. (For interpretation of the references to color in this figure legend, the reader is referred to the web version of this article.)

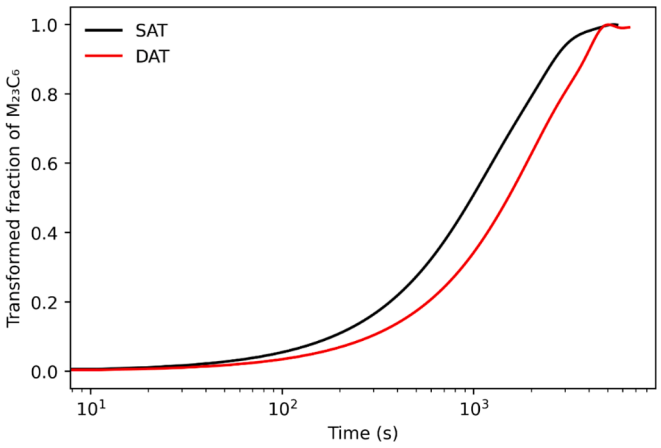

Fig. 14. Evolution of transformed fraction of $M_{23}C_6$ carbides during isothermal tempering at 520 °C. SAT in black and DAT in red. (For interpretation of the references to color in this figure legend, the reader is referred to the web version of this article.)

k is the rate constant and T is the absolute temperature, we obtained a linear relationship. From Fig. 15.b, the activation energies for the precipitation were calculated for both conditions and estimated at 88KJ/mol and 52KJ/mol, for SAT and DAT treatment, respectively. This is in agreement with values reported in the literature [66]. This means that, for the investigated steel, $M_{23}C_6$ carbides formation occurs via the self-diffusion of carbon atoms [67]. The activation energies are temperature and microstructure dependent. Since both SAT and DAT samples were tempered at the same temperature (i.e, 520°C), the differences in the activation energy could reasonably be attributed to the differences in the initial microstructures.

As reported in the variant analysis (see section3.1.2) DAT treatment resulted in a higher density of HAGBs and, consequently, an increased number of V1/V2 pairs. Studies have shown that the shape of $M_{23}C_6$ carbides and the precipitation sequence is intricately linked to grain boundary misorientation [25]. Although they have no direct physical significance, the values of the Avrami coefficients (n close to 1) suggest that precipitation takes place on lath, block, and grain boundaries. Thus, in the case of DAT, the presence of higher-density HAGBs may be one reason for the more homogeneous precipitation of carbides. This would also explain the slower incubation time. According to the extended volume concept, the evolution of the fraction during isothermal transformations could also be expressed as [57]:

$$f = V^{M23C6}/V^{T} = 1 - \exp\left(-\pi v_{M23C6}^{3} I_v t^4/3\right) \quad (5)$$

With V^{M23C6} the volume fraction of the carbides, V^{T} the total volume (matrix + carbide), v_{M23C6} the rate of growth of the $M_{23}C_6$ particles, t the time, and I_v the nucleation rate per unit volume, which depends on the number of nucleation sites. Assuming that the nucleated particles are spherical and their growth occurs isotropically at a constant rate, v_{M23C6}, it becomes straightforward to calculate $v_{M23C6}^{3} I_v$ from the plotted sigmoidal curve. From this, it can be deduced that the longer incubation time is likely due to the nucleation rate per unit volume, which, in turn, can be attributed to the presence of a greater number of nucleation sites in DAT samples compared to SAT samples.

Along with the longer incubation time, the lower activation energy found in the DAT samples attests that precipitation in DAT treatment requires a lower energy barrier and would occur more spontaneously. Once carbides start to precipitate after quenching, the abundant nucleation sites lead to short diffusion distances from the matrix, as the number of interfaces is increasing, and this makes the precipitation easier for DAT treatment compared to SAT treatment.

3.3. Mechanical properties

Fig. 16 shows and summarizes the measured mechanical properties. It indicates that DAT treatment improves impact toughness and wear resistance together while keeping the hardness values nearly identical. The results are consistent with those reported in the literature [68].

A high strength and wear resistance value is often accompanied by a low toughness value. According to Krauss and Roberts [2], CVN impact energy at room temperature values for conventionally manufactured cold work tool steels vary between 2 and 7 J. For modified A8 steel, an average value of almost 6 J therefore seems reasonable and in line with the results previously found [69].

The DAT specimens showed significant improvements in both

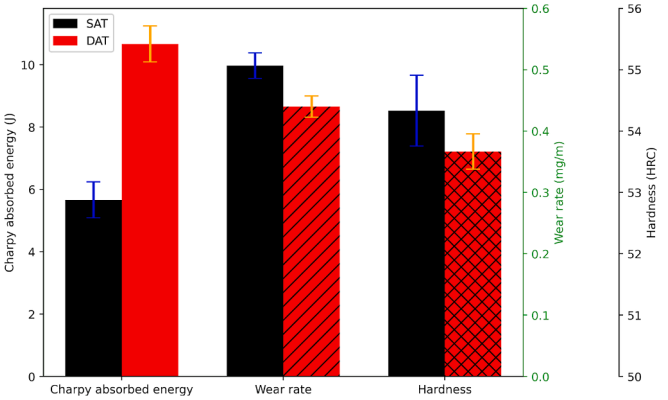

Fig. 16. Mechanical properties of quenched and tempered samples showing increased Charpy absorbed energy and reduced wear rate as a result of DAT heat treatment.

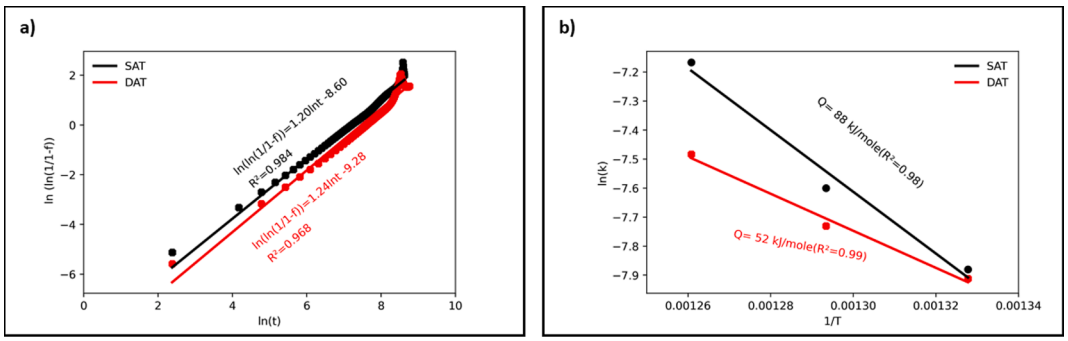

Fig. 15. Determination of kinetics parameters. (a) ln(ln(1/1-f)) against ln(t) to estimate the Avrami constants n and k_0 for tempering at 520 °C. (b) ln(k) against 1/T to determine the activation energy from the slope of the regression line. SAT in black and DAT in red. (For interpretation of the references to color in this figure legend, the reader is referred to the web version of this article.)

toughness and wear resistance. Notably, the CVN impact energy for DAT increased to 11 J, representing an 80 % enhancement compared to the SAT specimen. The sample's average wear rate was reduced to 0.45 mg/m and the conventionally heat-treated SAT samples had a 0.50 mg/m which means that that wear resistance was 10 % better in the DAT samples. Regarding the improvement in wear resistance, carbide size, distribution, and morphology are thought to be responsible for it.

The strengthening in steels with secondary phases originate from the contribution of several parallel mechanisms. As shown in Fig. 16, both SAT and DAT samples had similar hardness values, despite the fact that in the DAT samples a lower fraction of secondary carbides were present and therefore, lower hardness levels were to be expected. However, the reduction in the effective grain size (block width) along with the carbide refinement in the DAT samples, contributed to increase the hardness, thereby, keeping almost constant the level of hardness in these samples.

The improvement in CVN could be attributed to the variant pairing as shown in section 3.1.2 along with the finer dispersion of secondary carbides. To analyze fracture mechanisms, the fracture surfaces of the CVN specimens were observed under SEM, as shown in Fig. 17. The analysis revealed significant differences between the SAT and DAT samples, correlating with their respective Charpy impact energies.

In the SAT samples, small dimples were observed alongside quasi-cleavage areas and some cracks, with shear lips indicating a degree of brittle fracture. The fracture surface exhibited moderately deep and elongated dimples, with an average size of approximately 2 μm as determined by ImageJ analysis[70]. These dimples are characteristic of microvoid coalescence (MVC), a ductile fracture mechanism in which voids nucleate and grow around hard particles such as carbides[71].

It is important to emphasize, as highlighted by Fukaura et al. [72] and Jurci et al. [73] that carbides play a dual role in both crack initiation and propagation, depending on their size and distribution. Fine carbides, due to their small size and greater number, act as effective nucleation sites for microvoids. This facilitates the initiation of ductile fracture through MVC, resulting in a high density of small dimples and improved energy absorption. However, coarse or larger carbides (e.g. LSCs) act differently; they serve as local stress concentrators and are more susceptible to cracking themselves under applied stress. When a large carbide cracks, it can directly initiate a microcrack, which may then propagate into the matrix, facilitating brittle fracture modes such as cleavage or quasi-cleavage. Thus, the presence of large carbides not only affects the initiation of cracks but also provides easy pathways for crack propagation, reducing the overall fracture toughness.

In our SAT samples, the observation of both small dimples and quasi-cleavage features suggests that crack initiation occurs at both fine and coarse carbides. Fine carbides promote ductile MVC, while coarse carbides are likely sites for the initiation and propagation of brittle cracks, explaining the mixed fracture morphology.

In contrast, the DAT samples displayed a markedly different surface morphology, characterized by deeper and more elongated dimples (average 7 μm) and prominent tear ridges. This suggests that the DAT heat treatment resulted in a finer and more uniform carbide distribution. With fewer coarse carbides present, crack initiation is dominated by MVC at fine carbides, leading to more ductile fracture behavior and higher Charpy impact energy. The reduction in coarse carbides limits the number of sites available for brittle crack initiation and propagation, thereby enhancing toughness.

On the other hand, the improvement in wear resistance observed in our samples can be attributed to several microstructural factors, particularly the size, distribution, and morphology of carbides. Finer and more uniformly distributed SSCs act as effective barriers to crack propagation and micro-cutting during sliding, thereby limiting material removal. Additionally, a more spherical or carbide morphology tends to reduce local stress concentrations and lowers the risk of crack initiation.

Beyond the influence of carbides, the reduction in martensite block width also appears to play an important role in enhancing wear resistance. A finer block structure increases the density of interfaces, which hinders slip and the propagation of microcracks under mechanical stress. This further subdivision of the martensitic structure helps distribute stresses more evenly and improves local toughness, both of which contribute to limiting surface damage during wear tests as recently shown by Jia et al. [74].

4. Discussion

4.1. Effect of carbon content in solid solution on variant selection and carbide precipitation

The smaller volume contraction observed in the DAT samples from isothermal dilatometric curves could be associated with fewer available carbon atoms for precipitation as suggested by Waterschoot et al. [42]. Therefore, the higher fraction of secondary carbides in the SAT samples inevitably reduces the carbon content in the martensite matrix. Consequently, it is believed that more carbon is present in the matrix of the DAT samples compared to the SAT ones.

To measure the carbon content, an enlargement of the martensite a'(200) XRD pattern is displayed in Fig. 18. The martensite peak for the DAT samples tends to shift to the left compared to the SAT samples. Numerous studies have focused on the crystal structure of martensite and its tetragonality [75 76]. Honda and Nishiyama established a linear relationship between the c/a ratio and the carbon content (wt.%) [77], and it was long believed that no tetragonality existed for steels with less than 0.6 wt% carbon. However, Lu [78] recently showed that for carbon content less than 0.6 wt%, a deconvolution of the overlapped martensite a'(200) peak and a'(002) could provide an accurate estimate of the c/a ratio.

Fig. 18 reveals a left-tail XRD pattern for the DAT samples. This asymmetry indicates that the DAT martensite crystal contains more carbon atoms than the SAT one. Deconvolution was performed using

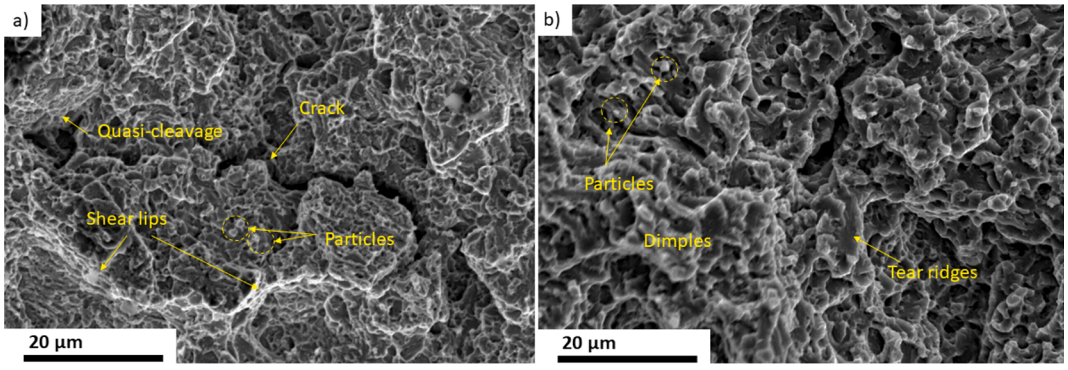

Fig. 17. SE-SEM Fractography of the propagation zones on Charpy V-notch samples: (a) SAT specimen showing cracks, shear lips and quasi-cleavage surfaces. (b) DAT specimen exhibiting elongated dimples and tear ridges from.

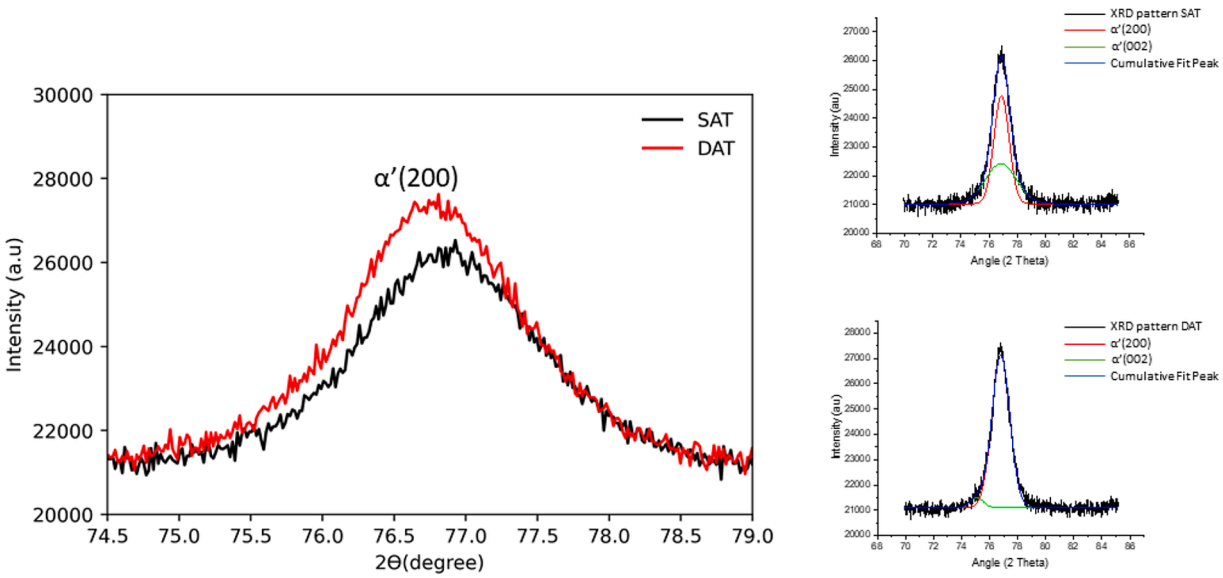

Fig. 18. Enlargement of peak a' (200) showing the left-tail in the DAT pattern. The SAT data are shown in black, the DAT data in red, along with the corresponding deconvoluted peaks. Deconvolution was performed using the Gaussian peak separation method. (For interpretation of the references to color in this figure legend, the reader is referred to the web version of this article.)

OriginPro software [79] and applying the Gaussian peak separation method. Results show the asymmetry causing the shift to lower diffraction angles, which could indicate a higher carbon content in the DAT samples. However, the c/a ratio could not be conclusively measured.

The carbon content in the matrix was estimated thus by using the equation developed by Bhadeshia [80]:

$$a_{BCC} = a_{Fe} + \left(3a_{Fe}^2\right)^{-1} \times \left[\left(a_{Fe} - 0.0279x_{c^a}\right)^2\left(a_{Fe} + 0.2496x_{c^a}\right) - a_{Fe}^3\right] - 0.003x_{Si^a} + 0.006x_{Mn^a} + 0.007x_{Ni^a} + 0.031x_{Mo^a} + 0.005x_{Cr^a} + 0.0096x_{V^a} \quad (6)$$

where a_{BCC} is the lattice parameter measured by the XRD, a_{Fe} is the lattice parameter of pure ferrite (0.28664 nm [27]) and x_{i^a} is the mole fraction of the element i in the matrix.

The lattice parameters measured from XRD are 0.28766 nm and 0.28779 nm for SAT and DAT, respectively. The carbon content in the martensite matrix in the DAT is estimated at 0.29 wt% which is slightly higher than in the SAT samples which is estimated at 0.26 wt%. These results align with the thermodynamic estimation from FactSage of the carbon content in austenite solid solution, shown in Fig. 19. The higher solubility in the DAT samples could be attributed to its thermodynamic stability, as carbon atoms are known to be more stable in defects (grain boundaries, dislocations, etc.) [81]. As shown in section 3.1.1, the DAT treatment increased the density of boundaries; therefore, it is reasonable to assume that a higher amount of carbon atoms was trapped in defects.

Carbon content significantly affects variant pairing and selection, as reported by several researchers [13,16,82]. Stormvinter et al. [13] indicated that increased carbon content effectively increases the number of V1/V2 variant pairs and shifts the transformation path from CP to Bain groups formation. Morito et al. [83] demonstrated that increased carbon content leads to the formation of sub-blocks within the same CP groups, increased density of V1/V2 variant pairs, and the formation of all possible 24 variants.

In the present work, variant analysis of grains showed that sub-blocks formed in the DAT samples for any PAGS, and all possible variants formed within a single PAG (G4, G5, and G6), regardless of the PAGS. For the SAT samples, however, a decrease in PAGS led to variant selection. The initial relationship between the PAGS and variant

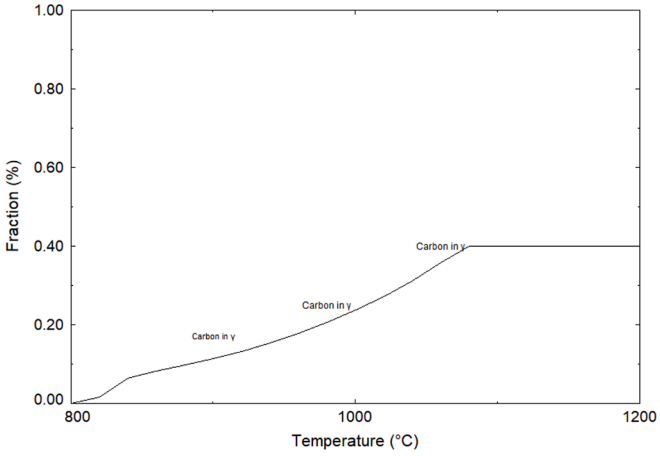

Fig. 19. Carbon content in austenite under equilibrium conditions, as determined by FactSage simulation.

selection, studied by Morito et al. [14], stipulated that only 1 CP group (with its corresponding variants) could appear in small grains, which was not the case in the DAT samples.

An additional observation in DAT samples, indicated that the block width did not significantly vary with the PAGS. This finding is in contrast with the commonly observed relationship where block width typically decreases with decreasing PAGS [12]. The relative invariance of block width across different PAGS in our study could be attributed to the higher carbon content in solid solution, especially in the DAT samples. As discussed above, increased carbon content promotes the formation of sub-blocks and refines the martensite structure, and this appears to counteract the influence of PAGS on block width as it was also suggested by Morito and coworkers [84]..

The carbon content in the matrix also affects the sequence of carbide precipitation during tempering. As continuous heating proceeds, the loss of martensite tetragonality begins as carbon atoms are released from the supersaturated lattice. This process coincides with the precipitation of transient ε-carbide, which is observed in the dilatometric curves of the SAT samples but not in the DAT samples. The formation of these transient carbides in SAT not only reduces the available carbon in the matrix

but also creates preferred nucleation sites for subsequent $M_{23}C_6$ precipitation. This promotes faster nucleation and growth of $M_{23}C_6$ in SAT, particularly along grain boundaries, leading to the formation of ESCs at these locations. According to Porter [85], accelerated thickening and lengthening of carbides at grain boundaries are facilitated by grain boundary diffusion, this explains why ESCs are mainly located at PAGBs. In contrast, the DAT samples, with their finer martensitic structure and higher HAGBs density, favor the uniform precipitation of more SSCs and do not show the formation of ESCs. The activation energies calculated for $M_{23}C_6$ precipitation in both samples also suggest that carbon self-diffusion controls the precipitation. The substructure inherited from quenching significantly impacts the kinetics of carbide precipitation, as also reported by Sun et al. [27]. According to Xu et al. [66], refinement of the martensite structure (lath and blocks) of the as-quenched microstructure reduces the activation energy of $M_{23}C_6$ precipitation during isothermal tempering. This is explained by the shorter diffusion distance for carbon atoms, resulting in a smaller energy barrier for precipitation.

4.2. Effect of double austenitization on carbon redistribution during quenching

Limited research is available on the characteristics of multiple austenitization cycles on martensite substructure. In addition to the increased carbon content in solid solution as discussed in the previous section, Hidalgo and Santofimia [86] reported that a second austenitization leads to a homogenous redistribution of carbon in the matrix. This mechanism could be another factor contributing to variant selection in some grains in the SAT samples. Indeed, because grains might have different growth kinetics, the probability of having a non-homogeneous distribution of carbon atoms in PAGs is higher. In larger grains (e.g., G1, G2), the concentration of carbon atoms might be higher, which could explain the formation of sub-block structures. In the DAT samples, however, a second austenitization seems not only to increase carbon content in austenite solid solution but also to redistribute it regardless of the PAGS.

To validate this hypothesis, dilatometric curves obtained after quenching from the austenite regions for both the SAT samples (1st quenching) and DAT samples (2nd quenching) were analyzed and reported in Fig. 20. Although an in-depth study of martensite formation kinetics is beyond the scope of this work, the derivative curves provide important insights into the carbon redistribution hypothesis. It must be noted that, in the present work, we have adopted the off-set method along with derivative curves for the analysis of the dilatometric data [87].

As shown in Fig. 20, upon quenching, the SAT samples show a discontinuous transformation starting around 360 °C down to 250 °C before undergoing a considerable volume change. This anomalous behavior in martensitic transformation has been a subject of recent interest, with studies focusing on the root causes for the observed discontinuities [88,89,90]. For the SAT samples, the presence of more than one martensite start temperature (M_s) is evidence of a multi-step transformation, initially possibly due to the presence of different PAGs with varying carbon contents in austenite solid solution. Low-carbon content PAGs will transform to martensite first at higher temperatures (starting around 360 °C), and as undercooling proceeds, more martensite forms. From 250 °C to 220 °C, the massive burst transformation of austenite to martensite begins at M_{s1}, while a second temperature M_{s2} is detected around 200 °C.

For the DAT samples, the first deviation from the cooling curve is observed around 338 °C, possibly due to some PAGs depleted in carbon. The burst transformation of austenite to martensite starts with a unique M_s, and no M_{s2} peak could be detected.

4.3. Origin of the multi-step martensitic transformation

The dilatometric results reported in Fig. 20 revealed that the martensitic transformation in SAT occurred in multiple stages, evidenced by the appearance of several M_s temperatures. Furthermore, as reported above (section 4.2), smaller grains, such as G3, which might contain less carbon, exhibit a greater variant selection and transform first, preceding the massive transformation. In contrast, larger grains (e.g., G1, G2) transform during the burst transformations. To investigate this further, we converted the dilatometric curves for each condition into kinetics curves. The onset of transformation for each condition was defined as the point where a minimal detection of length change occurred, corresponding to a 0.01 vol fraction transformation.

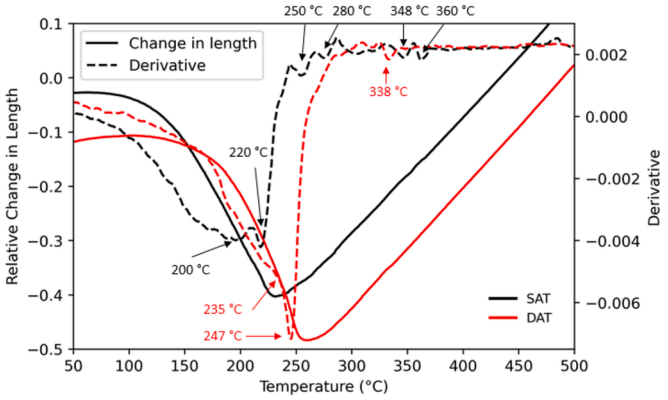

Fig. 20. Dilatometric curves showing the relative change in length (solid lines) versus temperature during quenching, along with their derivatives (dashed lines). Multiple martensite start (Ms) temperatures are indicated for the SAT samples prior to the burst transformation (highlighted with black arrows). The quenching curve for SAT is shown in black, while the second quenching for DAT is shown in red. (For interpretation of the references to color in this figure legend, the reader is referred to the web version of this article.)

Fig. 21a illustrates the evolution of martensite volume fraction ($f_{a'}$) as a function of undercooling ($\Delta T = M_s - T$). Notably, the DAT samples exhibit a more rapid evolution of the martensite fraction compared to the SAT ones. This observation is further corroborated by the transformation rate ($df_{a'}/dT$) as a function of undercooling, as shown in Fig. 21b. During the second austenitization, we observe that the transformation peak is reached more quickly and is twice as high as that of SAT. This accelerated transformation in DAT samples could be explained by the creation of numerous nucleation sites, leading to faster growth at the beginning of the transformation, as also reported in previous studies [91,92]. Conversely, SAT samples exhibit fewer nucleation sites, which explains the slower transformation rate and the lower peak.

When the necessary free energy is reached and transformation becomes possible, the first martensite crystal forms, initiating a cascade of martensitic transformation. Subsequent growth occurs through an autocatalytic phenomenon. The initial colonies that form have ample space to grow with few obstacles, promoting rapid growth. As more colonies form, the PAG becomes increasingly sectioned, restricting the space where new colonies can form. This phenomenon is known as mechanical stabilization of austenite [28], resulting in a drastic reduction in the transformation rate, as more effort is required for the remaining space to transform.

In the case of DAT samples, the transformation rate drops suddenly and continues to decrease as the transformation progresses while for SAT samples, after reaching the initial peak, there is a slight decrease, followed by a new increase which suggests that a new transformation has taken place. Mao et al. [89] associated the presence of these secondary and tertiary peaks to the occurrence of multiple martensitic transformations, i.e., multiple M_s temperatures. Fig. 21.c shows the transformation rate versus the martensite fraction. For DAT samples, the transformation rate starts to decrease after the formation of about 17 % martensite. In contrast, in SAT samples, approximately 10 % of martensite is formed during the first peak, followed by an additional 20

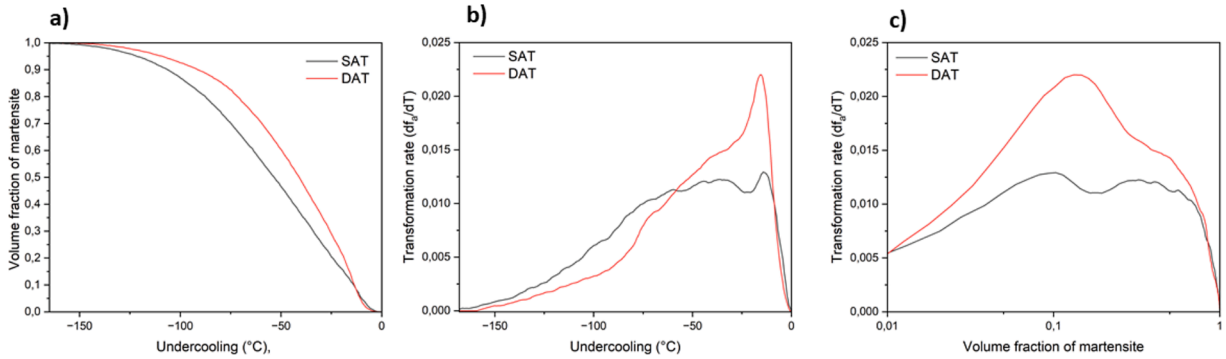

Fig. 21. (a) Volume fraction of martensite ($f_{a'}$) against undercooling ($\Delta T = M_s$-T). (b)Transformation rate of martensite ($df_{a'}/dT$) against undercooling. (c) Transformation rate against volume fraction of martensite.

% transformation at M_{s2} before the transformation rate begins to decrease.

Liu et al. [93], associated the appearance of multiple transformation stages with the occurrence of an auto-tempering process. Carbon atoms, rejected from newly formed martensite, enrich the lath boundaries and the untransformed austenite. However, this carbon-enriched untransformed austenite was already mechanically stabilized and therefore will transform at an even lower temperature. Based on the above mechanism, the auto-tempering process is accentuated at slower cooling rates.

On the other hand, Hutchinson et al. [94] reported that even at very high cooling rates (1000 K/s), carbon can diffuse over distances of 1.5 μm when the transformation begins below M_s. In the same study [94], for cooling rates of 10 K/s (close to the cooling rate used in the present work), diffusion distances of up to 20 μm were noted. This implies that in our case, carbon rejected by the first martensite laths can diffuse throughout the PAG. It is important to note that not all laths reject carbon equally. Using atom probe tomography (APT), Morsdorf and coworkers [48] demonstrated that coarse laths were more prone to rejecting carbon, with their carbon concentration being up to 5 times lower than the matrix, while finer laths showed less of this tendency. They also reported that these large laths, which generally have a flat contact surface with the PAGBs, are those that appear at the beginning of the martensitic transformation.

The above analysis confirms our experimental findings on variant analysis (section 3.1.2) where we observed two morphologies present in G1 and G2. In SAT, coarse laths were formed at the beginning of the transformation below Ms_1 and reject carbon into untransformed regions. This carbon enrichment of austenite is at the origin of a second transformation with an Ms_2. As reported in [13], an increase in carbon concentration favors the appearance of multiple variants. This could explain why regions of coarse laths are interspersed with regions of multiple multivariant laths. Notably, this carbon rejection from the matrix in SAT samples is could be also one reason why the α'(200) XRD peak seen in Fig. 18 does not show a left-tail and is symmetrical, as the matrix has rejected most of its carbon atoms to the untransformed γ_r. This symmetrical peak is a sign of losing tetragonality in the martensite structure. This would also explain why the C-enriched γ_r resisted to transformation during tempering in the SAT samples.

In the DAT samples, the greater number of nucleation sites facilitates the appearance of multiple variants that have a flat contact surface with the PAGBs from the start of the transformation. The higher and more homogeneously redistributed carbon content leads to a more homogeneous martensitic transformation characterized by fine laths that do not reject carbon at the beginning of the transformation, explaining the absence of M_{s2}.

Based on the above results and discussion, the following mechanisms could be operating for the two investigated heat treatments and are schematically represented in Fig. 22:

1) For the SAT treatment, austenitization leads to different populations of PAGs with varying carbon contents, with larger grains having more carbon in solid solution than the smaller ones. During cooling, these different populations of PAGs transform at different temperatures, which also implies variant selection in small grains and the disappearance of sub-block structures.

2) For the DAT samples: The PAG is homogeneously enriched in carbon throughout the sample, and upon cooling, a continuous martensitic transformation occurs. The higher carbon content leads to the formation of sub-blocks in the different CP groups and promotes HAGBs variant pairs along with the formation of all 24 possible variants.

The above findings reveal that higher carbon content in solid solution promotes the formation of sub-blocks within martensite packets and increases the density of HAGBs, which are crucial for enhancing mechanical properties. Notably, the double austenitization leads to a more homogeneous carbon redistribution compared to single austenitization, resulting in a more uniform single-stage martensite transformation and the formation of a substructure that is less sensitive to the PAGS. This uniformity is reflected in the near-constant block width observed in DAT samples for various grain sizes, contrasting with the traditional PAGS-dependent block width, seen in SAT samples.

The complex interplay between carbon content in the as-quenched martensite and carbide precipitation during tempering must also be taken into account. The fact that DAT samples, despite having more potential nucleation sites and a lower activation energy for $M_{23}C_6$ precipitation (52 kJ/mol compared to 88 kJ/mol for SAT) show less carbide precipitation and a longer incubation time, suggests that more carbon atoms remain stable in the martensite matrix, likely due to the increased density of defects acting as carbon traps. In addition, the homogeneous redistribution of carbon atoms in the matrix in DAT samples leads to a more uniform distribution of carbides after tempering. This is in contrast to SAT samples, where carbon segregation across different grains tends to manifest in enriched-carbide zones with aggregates of carbides and carbide-free zones, as reported in our recent work [35].

These microstructural alterations resulting from DAT have significant implications for the mechanical properties. The impact toughness of the DAT samples was notably improved, as evidenced by the fracture surface analysis. Furthermore, the wear resistance was enhanced due to the spherical and homogeneous carbide precipitation observed in the DAT samples. This uniform distribution of spherical carbides, coupled with the more homogeneous martensite structure, contributes to a more consistent and superior wear performance compared to the SAT samples.

This correlation offers a pathway to optimize steel properties, making it possible to achieve a balance between high wear resistance and high toughness. To further advance these findings, several avenues for future research are identified. Although grain refinement and increased carbon content in solution were observed, the overall hardness levels remained unchanged. This phenomenon may be related to the presence of nanoscale carbides, which are known to contribute significantly to secondary hardening but were not characterized in the present study.

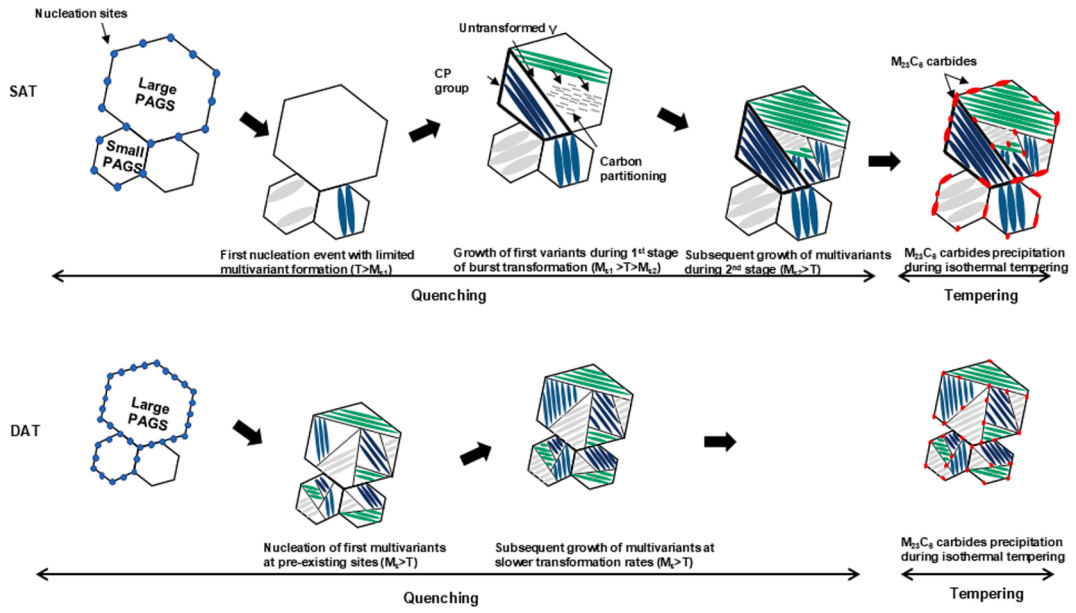

Fig. 22. Schematic illustration of the lath martensite transformation sequence in the investigated steel during quenching, followed by $M_{23}C_6$ carbide precipitation during isothermal tempering for both SAT and DAT conditions. The left figures depict the PAG structure during quenching, prior to martensite formation, with blue dots indicating martensite nucleation sites. Laths of the same color correspond to the same CP group. Red particles represent $M_{23}C_6$ carbides formed during tempering. (For interpretation of the references to color in this figure legend, the reader is referred to the web version of this article.)

Further investigations using TEM are planned to analyze these nanostructural features in detail.

In addition, while direct evidence of multi-step martensitic transformation was not obtained in this work, advanced characterization techniques such as APT could provide valuable insights into these transformation mechanisms in future studies. Finally, the three-dimensional crystallographic features of the microstructure were not explored here and represent a promising direction for future research, which could provide a more comprehensive understanding of the relationships between processing, microstructure, and properties.

5. Conclusions

The effects of double austenitization and tempering (DAT) on the microstructure, mechanical properties, and precipitation kinetics of a modified AISI A8 tool steel were investigated and compared to the conventional single austenitization and tempering (SAT). Using high-resolution dilatometry and advanced electron microscopy techniques, we identified the key mechanisms underlying the observed improvements in impact strength and wear resistance. The main findings of this research are summarized as follows:

- Microstructural refinement: DAT treatment effectively refined the overall microstructure, reducing the prior austenite grain size (PAGS), packet size, and block width compared to SAT treatment.
- Variant pairs regulation: DAT led to a significant reduction in the fraction of V1/V4 Low angle grain boundaries (LAGBs) and an increase in V1/V2 block boundaries. This shift towards a higher density of High angle grain boundaries (HAGBs) contributed to enhanced matrix toughness.
- Enhanced carbon redistribution: DAT increased the carbon content in martensite and enhanced its redistribution across the different Prior austenite grains (PAGs). This promoted the formation of K-S multivariant within single PAGs, regardless of the PAGS.
- Martensite transformation kinetics: The DAT treatment resulted in a more rapid and uniform martensitic transformation compared to SAT, characterized by a single, higher transformation rate peak. This is primarily due to increased nucleation sites and a more homogeneous carbon distribution.
- Alloy carbide refinement: The redistribution of carbon and its retention in the martensitic matrix along with the increased density of nucleation sites favored the precipitation of homogenous spherical $M_{23}C_6$ carbides during tempering.

The findings of the present work provide valuable insights into the mechanisms of microstructure evolution and property enhancement in high-performance tool steels subjected to complex heat treatments. Furthermore, they establish a foundation for tailoring heat treatments in other steel grades to achieve specific combinations of mechanical properties.

CRediT authorship contribution statement

Hamza Sofiane Meddas: Writing – review & editing, Writing – original draft, Visualization, Validation, Software, Methodology, Investigation, Formal analysis, Data curation. **Muftah Zorgani:** Writing – review & editing, Visualization, Supervision, Software, Methodology, Investigation, Data curation. **Majid Heidari:** Writing – review & editing, Project administration, Methodology, Investigation, Formal analysis. **Mousa Javidani:** Writing – review & editing, Visualization, Validation, Supervision. **Tom Levasseur:** Writing – review & editing, Resources, Project administration, Funding acquisition, Conceptualization. **Mohammad Jahazi:** Writing – review & editing, Visualization, Validation, Supervision, Resources, Project administration, Methodology, Investigation, Funding acquisition, Formal analysis, Conceptualization.

Declaration of competing interest

The authors declare the following financial interests/personal relationships which may be considered as potential competing interests: Hamza Sofiane Meddas reports administrative support and writing assistance were provided by DKSPEC. Majid Heidari, Tom Levasseur reports a relationship with DKSPEC that includes: employment. If there are other authors, they declare that they have no known competing financial interests or personal relationships that could have appeared to

influence the work reported in this paper.

Acknowledgments

The authors would like to thank the Natural Sciences and Engineering Research Council of Canada (NSERC), Consortium de Recherche et Innovation en Transformation Métallique (CRITM), and the industrial partners of the project DK-Spec, Québec, Canada and Forezienne, France for their support and financial contribution under the Grant No. ALLRP 571323-21.

Data availability

The data that has been used is confidential.

References

[1] W.E. Bryson, *Heat treatment, selection, and application of tool steels*, Hanser Gardner Publications, Cincinnati, 2005.
[2] G.A. Roberts, R. Kennedy, G. Krauss, *Tool steels*, ASM Int. (1998).
[3] V. Mbakop Nanshie, A. Aidibe, M. Heidari, M. Jahazi, *Impact of coating and microstructure on wear resistance of tool steels for wood cutting: a novel approach to quantification and analysis of wear-related damages*, J. Wood Sci. 70 (1) (2024) 20, https://doi.org/10.1186/s10086-024-02132-6.
[4] N. Pillai, R. Karthikeyan, S. Kannan, S. Vincent, *Effect of Cryogenic treatment on VIKING cold working tool steel and development of wear mechanism maps*, Procedia Manuf. 26 (2018) 329–342, https://doi.org/10.1016/j.promfg.2018.07.041.
[5] S.C. Ghosh, M. Heidari, R.E. Hernández, C. Blais, *Patterns of knife edge recession in an industrial chipper-canter*, For. Prod. J. 65 (7–8) (2015) 358–364, https://doi.org/10.13073/FPJ-D-14-00057.
[6] T. Matsuno, K. Nakagiri, T. Matsuda, T. Tanaka, T. Yasutomi, H. Shoji, M. Ohata, *Identification of ductile fracture design curve for hardened quasi-brittle AISI-D2 tool steel to predict shearing tool failure*, J. Mater. Process. Technol. 307 (2022) 117680, https://doi.org/10.1016/j.jmatprotec.2022.117680.
[7] L.K. Katiyar, C. Sasikumar, *Development of hard and tough tool steel through precipitation of ultrafine carbides from super saturated solid solution*, Mater. Today Proc. 66 (2022) 3822–3829, https://doi.org/10.1016/j.matpr.2022.06.251.
[8] M. Randelius, Influence of Microstructure on Fatigue and Ductility Properties of Tool Steels, KTH Royal Institute of Technology, Stockholm, Sweden, 2008. PhD Thesis.
[9] A. Heydari, A. Zarei-Hanzaki, M. Mahmoudi, A. Moshiri, M. Jaskari, L. Karjalainen, H. Balanian, H. Abedi, *Small crack growth behavior and correlated microstructure-sensitivity during cyclic deformation of a high-chromium/carbon wrought tool steel*, Mater. Sci. Eng. A 905 (2024) 146650, https://doi.org/10.1016/j.msea.2024.146650.
[10] T. Maki, *Morphology and substructure of martensite in steels*, Phase Transformat. Steels (2012) 34–58, https://doi.org/10.1533/9780857096111.1.34.
[11] S. Morito, X. Huang, T. Furuhara, T. Maki, N. Hansen, *The morphology and crystallography of lath martensite in alloy steels*, Acta Mater. 54 (19) (2006) 5323–5331, https://doi.org/10.1016/j.actamat.2006.07.009.
[12] S. Morito, H. Yoshida, T. Maki, X. Huang, *Effect of block size on the strength of lath martensite in low carbon steels*, Mater. Sci. Eng. A 438 (2006) 237–240, https://doi.org/10.1016/j.msea.2005.12.048.
[13] A. Stormvinter, G. Miyamoto, T. Furuhara, P. Hedström, A. Borgenstam, *Effect of carbon content on variant pairing of martensite in Fe–C alloys*, Acta Mater. 60 (20) (2012) 7265–7274, https://doi.org/10.1016/j.actamat.2012.09.046.
[14] S. Morito, H. Saito, T. Ogawa, T. Furuhara, T. Maki, *Effect of austenite grain size on the morphology and crystallography of lath martensite in low carbon steels*, ISIJ Int. 45 (1) (2005) 91–94, https://doi.org/10.2355/isijinternational.45.91.
[15] B. Wang, N. Chen, Y. Cai, W. Guo, M. Wang, *Effect of crystallographic features on low-temperature fatigue ductile-to-brittle transition for simulated coarse-grained heat-affected zone of bainite steel weld*, Int. J. Fatigue 170 (2023) 107523, https://doi.org/10.1016/j.ijfatigue.2023.107523.
[16] X. Wang, X. Ma, Z. Wang, S. Subramanian, Z. Xie, C. Shang, X. Li, *Carbon microalloying effect of base material on variant selection in coarse grained heat affected zone of X80 pipeline steel*, Mater Charact 149 (2019) 26–33, https://doi.org/10.1016/j.matchar.2019.01.005.
[17] B. Wu, Z. Wang, X. Wang, W. Xu, C. Shang, R. Misra, *Toughening of martensite matrix in high strength low alloy steel: regulation of variant pairs*, Mater. Sci. Eng. A 759 (2019) 430–436, https://doi.org/10.1016/j.msea.2019.05.030.
[18] X. Wang, Z. Wang, L. Dong, C. Shang, X. Ma, S. Subramanian, *New insights into the mechanism of cooling rate on the impact toughness of coarse grained heat affected zone from the aspect of variant selection*, Mater. Sci. Eng. A 704 (2017) 448–458, https://doi.org/10.1016/j.msea.2017.07.095.
[19] J. Li, C. Zhang, B. Jiang, L. Zhou, Y. Liu, *Effect of large-size M23C6-type carbides on the low-temperature toughness of martensitic heat-resistant steels*, J. Alloy. Compd. 685 (2016) 248–257, https://doi.org/10.1016/j.jallcom.2016.05.294.
[20] M. Muhammed, M. Javidani, M. Heidari, M. Jahazi, *Enhancing the tribological performance of tool steels for wood-processing applications: a comprehensive review*, Metals 13 (8) (2023) 1460, https://doi.org/10.3390/met13081460.
[21] A. Kipelova, A. Belyakov, R. Kaibyshev, *The crystallography of M23C6 carbides in a martensitic 9% Cr steel after tempering, aging and creep*, Phil. Mag. 93 (18) (2013) 2259–2268, https://doi.org/10.1080/14786435.2013.765995.
[22] H. Ghassemi Armaki, R. Chen, K. Maruyama, M. Igarashi, *Creep behavior and degradation of subgrain structures pinned by nanoscale precipitates in strength-enhanced 5 to 12áPct Cr ferritic steels*, Metall. Mater. Trans. A 42 (2011) 3084–3094, https://doi.org/10.1007/s11661-011-0726-8.
[23] J. Hidalgo, M. Vittorietti, H. Farahani, F. Vercruysse, R. Petrov, J. Sietsma, *Influence of M23C6 carbides on the heterogeneous strain development in annealed 420 stainless steel*, Acta Mater. 200 (2020) 74–90, https://doi.org/10.1016/j.actamat.2020.08.072.
[24] H. Hong, B. Rho, S.W. Nam, *Correlation of the M23C6 precipitation morphology with grain boundary characteristics in austenitic stainless steel*, Mater. Sci. Eng. A 318 (1–2) (2001) 285–292, https://doi.org/10.1016/S0921-5093(01)01254-0.
[25] B. Tang, L. Jiang, R. Hu, Q. Li, *Correlation between grain boundary misorientation and M23C6 precipitation behaviors in a wrought Ni-based superalloy*, Mater Charact 78 (2013) 144–150, https://doi.org/10.1016/j.matchar.2013.02.006.
[26] Y. Xu, X. Zhang, Y. Tian, C. Chen, Y. Nan, H. He, M. Wang, *Study on the nucleation and growth of M23C6 carbides in a 10% Cr martensite ferritic steel after long-term aging*, Mater Charact 111 (2016) 122–127, https://doi.org/10.1016/j.matchar.2015.11.023.
[27] C. Sun, P.-X. Fu, X.-P. Ma, H.-H. Liu, N.-Y. Du, Y.-F. Cao, H.-W. Liu, D.-Z. Li, *Effect of matrix carbon content and lath martensite microstructures on the tempered precipitates and impact toughness of a medium-carbon low-alloy steel*, J. Mater. Res. Technol. 9 (4) (2020) 7701–7710, https://doi.org/10.1016/j.jmrt.2020.05.002.
[28] T. Furuhara, K. Kikumoto, H. Saito, T. Sekine, T. Ogawa, S. Morito, T. Maki, *Phase transformation from fine-grained austenite*, ISIJ Int. 48 (8) (2008) 1038–1045, https://doi.org/10.2355/isijinternational.48.1038.
[29] R. Grange, *The rapid heat treatment of steel*, Metallurg. Trans. 2 (1) (1971) 65–78, https://doi.org/10.1007/BF02662639.
[30] K. Balan, A.V. Reddy, D. Sarma, *Effect of single and double austenitization treatments on the microstructure and mechanical properties of 16Cr-2Ni steel*, J. Mater. Eng. Perform. 8 (1999) 385–393, https://doi.org/10.1361/105994999770346963.
[31] T. Karthikeyan, V.T. Paul, S. Saroja, A. Moitra, G. Sasikala, M. Vijayalakshmi, *Grain refinement to improve impact toughness in 9Cr–1Mo steel through a double austenitization treatment*, J. Nucl. Mater. 419 (1–3) (2011) 256–262, https://doi.org/10.1016/j.jnucmat.2011.08.010.
[32] Q. Gao, Z. Yuan, Q. Ma, L. Yu, H. Li, *Strengthening and toughening optimizations of novel G115 martensitic steel: Utilizing secondary normalizing process*, Mater. Sci. Eng. A 852 (2022) 143621, https://doi.org/10.1016/j.msea.2022.143621.
[33] S. Salunkhe, D. Fabijanic, J. Nayak, P. Hodgson, *Effect of single and double austenitization treatments on the microstructure and hardness of AISI D2 tool steel*, Mater. Today Proc. 2 (4–5) (2015) 1901–1906, https://doi.org/10.1016/j.matpr.2015.07.145.
[34] J. Liu, H. Yu, T. Zhou, C. Song, K. Zhang, *Effect of double quenching and tempering heat treatment on the microstructure and mechanical properties of a novel 5Cr steel processed by electro-slag casting*, Mater. Sci. Eng. A 619 (2014) 212–220, https://doi.org/10.1016/j.msea.2014.09.063.
[35] H.S. Meddas, M. Zorgani, M. Heidari, M. Javidani, T. Levasseur, M. Jahazi, *Enhanced durability of wood cutting tools through thermal cycling*, Materials 17 (20) (2024) 5051, https://doi.org/10.3390/ma17205051.
[36] B. Ögel, E. Tekin, *The effect of double austenitization on the microstructure and fracture toughness of AISI M2 high speed steel*, Steel Res. 69 (6) (1998) 247–252, https://doi.org/10.1002/srin.199805544.
[37] M. Ali, D. Porter, J. Kömi, M. Eissa, T. Mattar, *The effect of double austenitization and quenching on the microstructure and mechanical properties of CrNiMoWMnV ultrahigh-strength steels after low-temperature tempering*, Mater. Sci. Eng. A 763 (2019) 138169, https://doi.org/10.1016/j.msea.2019.138169.
[38] C.W. Bale, P. Chartrand, S. Degterov, G. Eriksson, K. Hack, R.B. Mahfoud, J. Melançon, A. Pelton, S. Petersen, *FactSage thermochemical software and databases*, Calphad 26 (2) (2002) 189–228, https://doi.org/10.1016/S0364-5916(02)00035-4.
[39] D. Andrés, F. Caballero, C. Capdevila, D. San Martın, *Revealing austenite grain boundaries by thermal etching: advantages and disadvantages*, Mater Charact 49 (2) (2002) 121–127, https://doi.org/10.1016/S1044-5803(03)00002-0.
[40] F. Bachmann, R. Hielscher, H. Schaeben, *Texture analysis with MTEX–free and open source software toolbox*, Solid State Phenom. 160 (2010) 63–68, https://doi.org/10.4028/www.scientific.net/SSP.160.63.
[41] B. Deng, Y. Shi, F. Yuan, *Investigation on the structural origin of low thermal expansion coefficient of fused silica*, Materialia 12 (2020) 100752, https://doi.org/10.1016/j.mtla.2020.100752.
[42] T. Waterschoot, K. Verbeken, *Tempering kinetics of the martensitic phase in DP steel*, ISIJ Int. 46 (1) (2006) 138–146, https://doi.org/10.2355/isijinternational.46.138.
[43] J. Christian, *The theory of transformations in metals and alloys*, Newnes (2002), https://doi.org/10.1016/S1369-7021(03)00335-3.
[44] *Standard test methods for notched bar impact testing of metallic materials.* 2008. DOI: 10.1520/E0023-24.
[45] ASTM, G., *65. Standard test method for measuring abrasion using the dry sand/rubber wheel apparatus.* ASTM International, West Conshohocken, PA, 2000.
[46] R. Hielscher, T. Nyyssönen, F. Niessen, A.A. Gazder, *The variant graph approach to improved parent grain reconstruction*, Materialia 22 (2022) 101399, https://doi.org/10.1016/j.mtla.2022.101399.
[47] F. Niessen, T. Nyyssönen, A.A. Gazder, R. Hielscher, *Parent grain reconstruction from partially or fully transformed microstructures in MTEX*, J. Appl. Cryst. 55 (1) (2022), https://doi.org/10.1107/S1600576721011560.

[48] L. Morsdorf, C.C. Tasan, D. Ponge, D. Raabe, *3D structural and atomic-scale analysis of lath martensite: effect of the transformation sequence*, Acta Mater. 95 (2015) 366–377, https://doi.org/10.1016/j.actamat.2015.05.023.

[49] D. Das, A.K. Dutta, K.K. Ray, *Sub-zero treatments of AISI D2 steel: Part I. Microstructure and hardness*, Mater. Sci. Eng. A 527 (9) (2010) 2182–2193, https://doi.org/10.1016/j.msea.2009.10.070.

[50] P. Jurči, M. Dománková, Ľ. Čaplovič, J. Ptačinová, J. Sobotová, P. Salabová, O. Prikner, B. Šuštaršič, D. Jenko, *Microstructure and hardness of sub-zero treated and no tempered P/M Vanadis 6 ledeburitic tool steel*, Vacuum 111 (2015) 92–101, https://doi.org/10.1016/j.vacuum.2014.10.004.

[51] V. Gavriljuk, W. Theisen, V. Sirosh, E. Polshin, A. Kortmann, G. Mogilny, Y. N. Petrov, Y.V. Tarusin, *Low-temperature martensitic transformation in tool steels in relation to their deep cryogenic treatment*, Acta Mater. 61 (5) (2013) 1705–1715, https://doi.org/10.1016/j.actamat.2012.11.045.

[52] D. Shtansky, K. Nakai, Y. Ohmori, *Decomposition of martensite by discontinuous-like precipitation reaction in an Fe–17Cr–0.5 C alloy*, Acta Mater. 48 (4) (2000) 969–983, https://doi.org/10.1016/S1359-6454(99)00364-X.

[53] T. Nykiel, T. Hryniewicz, *Transformations of carbides during tempering of D3 tool steel*, J. Mater. Eng. Perform. 23 (2014) 2050–2054, https://doi.org/10.1007/s11665-014-0979-7.

[54] J. Ďurica, J. Ptačinová, M. Dománková, L. Čaplovič, M. Čaplovičová, L. Hrušovská, V. Malovcová, P. Jurči, *Changes in microstructure of ledeburitic tool steel due to vacuum austenitizing and quenching, sub-zero treatments at− 140 C and tempering*, Vacuum 170 (2019) 108977, https://doi.org/10.1016/j.vacuum.2019.108977.

[55] E. Pippel, J. Woltersdorf, G. Pöckl, G. Lichtenegger, *Microstructure and nanochemistry of carbide precipitates in high-speed steel S 6-5-2-5*, Mater Charact 43 (1) (1999) 41–55, https://doi.org/10.1016/S1044-5803(99)00003-0.

[56] H. Kim, J.-Y. Kang, D. Son, T.-H. Lee, K.-M. Cho, *Evolution of carbides in cold-work tool steels*, Mater Charact 107 (2015) 376–385, https://doi.org/10.1016/j.matchar.2015.08.001.

[57] H. Bhadeshia, R. Honeycombe, *Steels: Microstructure and Properties*, fourth ed.:, Butterworth-Heinemann, 2017.

[58] L. Cheng, C. Brakman, B. Korevaar, E. Mittemeijer, *The tempering of iron-carbon martensite; dilatometric and calorimetric analysis*, Metall. Trans. A 19 (1988) 2415–2426, https://doi.org/10.1007/BF02645469.

[59] M. Van Genderen, M. Isac, A. Böttger, E. Mittemeijer, *Aging and tempering behavior of iron-nickel-carbon and iron-carbon martensite*, Metall. Mater. Trans. A 28 (1997) 545–561, https://doi.org/10.1007/s11661-997-0042-5.

[60] W. Cui, D. San-Martín, P.E. Rivera-Díaz-del-Castillo, *Stability of retained austenite in martensitic high carbon steels. Part I: thermal stability*, Mater. Sci. Eng. A 711 (2018) 683–695, https://doi.org/10.1016/j.msea.2017.10.102.

[61] Y. Hirotsu, S. Nagakura, *Crystal structure and morphology of the carbide precipitated from martensitic high carbon steel during the first stage of tempering*, Acta Metall. 20 (4) (1972) 645–655, https://doi.org/10.1016/0001-6160(72)90020-X.

[62] J. Pacyna, *Dilatometric investigations of phase transformations at heating and cooling of hardened, unalloyed, high carbon steels*, J. Achievem. Mater. Manuf. Eng. 46 (1) (2011) 7–17.

[63] A. Barrow, J.-H. Kang, P. Rivera-Díaz-del-Castillo, *The ∈→ η→ θ transition in 100Cr6 and its effect on mechanical properties*, Acta Mater. 60 (6–7) (2012) 2805–2815, https://doi.org/10.1016/j.actamat.2012.01.046.

[64] C. Lerchbacher, S. Zinner, H. Leitner, *Direct or indirect: Influence of type of retained austenite decomposition during tempering on the toughness of a hot-work tool steel*, Mater. Sci. Eng. A 564 (2013) 163–168, https://doi.org/10.1016/j.msea.2012.11.105.

[65] A.S. Podder, H. Bhadeshia, *Thermal stability of austenite retained in bainitic steels*, Mater. Sci. Eng. A 527 (7–8) (2010) 2121–2128, https://doi.org/10.1016/j.msea.2009.11.063.

[66] L. Xu, D. Zhang, Y. Liu, B. Ning, Z. Qiao, Z. Yan, H. Li, *Precipitation kinetics of M23C6 in T/P92 heat-resistant steel by applying soft-impingement correction*, J. Mater. Res. 28 (11) (2013) 1529–1537, https://doi.org/10.1557/jmr.2013.116.

[67] J. Robson, H. Bhadeshia, *Modelling precipitation sequences in power plant steels Part 1–Kinetic theory*, Mater. Sci. Technol. 13 (8) (1997) 631–639, https://doi.org/10.1179/mst.1997.13.8.631.

[68] A. Darvishi, A. Daneshmayeh, A. Salehi, M. Ahmadi, *Effect of double austenitization on the microstructure and hardness of high-carbon steel 1.4% C–11.7% Cr*, Met. Sci. Heat Treat. 64 (1–2) (2022) 16–19, https://doi.org/10.1007/s11041-022-00755-4.

[69] M. Heidari, Improvement of Cutting Tool Life for the Primary Transformation of Wood, Université Laval, Québec, QC, Canada, 2019. Ph.D. Thesis.

[70] T.J. Collins, *ImageJ for microscopy*, Biotechniques 43 (S1) (2007) S25–S30, https://doi.org/10.2144/000112505.

[71] W.T. Becker, R.J. Shipley, *Failure analysis and prevention*, ASM Int. (2002), https://doi.org/10.31399/asm.hb.v11.9781627081801.

[72] K. Fukaura, Y. Yokoyama, D. Yokoi, N. Tsujii, K. Ono, *Fatigue of cold-work tool steels: effect of heat treatment and carbide morphology on fatigue crack formation, life, and fracture surface observations*, Metall. Mater. Trans. A 35 (2004) 1289–1300, https://doi.org/10.1007/s11661-004-0303-5.

[73] P. Jurči, J. Ptačinová, I. Dlouhý, *Fracture micro mechanism of cryogenically treated ledeburitic tool steel*, Lecture Notes Mech. Eng. (2022), https://doi.org/10.1007/978-981-16-8810-2_6.

[74] D. Jia, C. Zhang, R. Dong, H. Zhang, X. Gao, X. Feng, Z. Yang, F. Zhang, *Driving martensitic transformation through pre-cold deformation: unveiling the mechanism of microstructural evolution in martensite bearing steel*, Mater. Des. 252 (2025) 113788, https://doi.org/10.1016/j.matdes.2025.113788.

[75] O.D. Sherby, J. Wadsworth, D.R. Lesuer, C.K. Syn, *Revisiting the structure of martensite in iron-carbon steels*, Mater. Trans. 49 (9) (2008) 2016–2027, https://doi.org/10.2320/matertrans.MRA2007338.

[76] G. Krauss, *Martensite in steel: strength and structure*, Mater. Sci. Eng. A 273 (1999) 40–57, https://doi.org/10.1016/s0921-5093(99)00288-9.

[77] Z. Nishiyama, *Martensitic Transformation*, Elsevier, 2012.

[78] Y. Lu, H. Yu, R.D. Sisson Jr, *The effect of carbon content on the c/a ratio of as-quenched martensite in Fe-C alloys*, Mater. Sci. Eng. A 700 (2017) 592–597, https://doi.org/10.1016/j.msea.2017.05.094.

[79] E. Seifert, *OriginPro 9.1: scientific data analysis and graphing software-software review*, J. Chem. Inf. Model. 54 (5) (2014) 1552, https://doi.org/10.1021/ci500161d.

[80] H. Bhadeshia, S. David, J. Vitek, R. Reed, *Stress induced transformation to bainite in Fe–Cr–Mo–C pressure vessel steel*, Mater. Sci. Technol. 7 (8) (1991) 686–698, https://doi.org/10.1179/mst.1991.7.8.686.

[81] M. Maalekian, E. Kozeschnik, *A thermodynamic model for carbon trapping in lattice defects*, Calphad 32 (4) (2008) 650–654, https://doi.org/10.1016/j.calphad.2008.09.004.

[82] X. Wang, Z. Wang, X. Ma, S. Subramanian, Z. Xie, C. Shang, X. Li, *Analysis of impact toughness scatter in simulated coarse-grained HAZ of E550 grade offshore engineering steel from the aspect of crystallographic structure*, Mater Charact 140 (2018) 312–319, https://doi.org/10.1016/j.matchar.2018.03.037.

[83] S. Morito, H. Tanaka, R. Konishi, T. Furuhara, Maki, *The morphology and crystallography of lath martensite in Fe-C alloys*, Acta Mater. 51 (6) (2003) 1789–1799, https://doi.org/10.1016/S1359-6454(02)00577-3.

[84] S. Morito, Y. Edamatsu, K. Ichinotani, T. Ohba, T. Hayashi, Y. Adachi, T. Furuhara, G. Miyamoto, N. Takayama, *Quantitative analysis of three-dimensional morphology of martensite packets and blocks in iron-carbon-manganese steels*, J. Alloy. Compd. 577 (2013) S587–S592, https://doi.org/10.1016/j.jallcom.2012.02.004.

[85] D.A. Porter, K.E. Easterling, *Phase Transformations in Metals and Alloys (revised reprint)*, CRC Press, 2009.

[86] J. Hidalgo, M.J. Santofimia, *Effect of prior austenite grain size refinement by thermal cycling on the microstructural features of as-quenched lath martensite*, Metall. Mater. Trans. A 47 (2016) 5288–5301, https://doi.org/10.1007/s11661-016-3525-4.

[87] H.-S. Yang, H. Bhadeshia, *Uncertainties in dilatometric determination of martensite start temperature*, Mater. Sci. Technol. 23 (5) (2007) 556–560, https://doi.org/10.1179/174328407X176857.

[88] M. Villa, K. Pantleon, M. Reich, O. Kessler, M.A. Somers, *Kinetics of anomalous multi-step formation of lath martensite in steel*, Acta Mater. 80 (2014) 468–477, https://doi.org/10.1016/j.actamat.2014.08.031.

[89] C. Mao, C. Liu, L. Yu, H. Li, Y. Liu, *Discontinuous lath martensite transformation and its relationship with annealing twin of parent austenite and cooling rate in low carbon RAFM steel*, Mater. Des. 197 (2021) 109252, https://doi.org/10.1016/j.matdes.2020.109252.

[90] S. Loewy, B. Rheingans, S.R. Meka, E.J. Mittemeijer, *Unusual martensite-formation kinetics in steels: Observation of discontinuous transformation rates*, Acta Mater. 64 (2014) 93–99, https://doi.org/10.1016/j.actamat.2013.11.052.

[91] C. Celada-Casero, J. Sietsma, M.J. Santofimia, *The role of the austenite grain size in the martensitic transformation in low carbon steels*, Mater. Des. 167 (2019) 107625, https://doi.org/10.1016/j.matdes.2019.107625.

[92] H.-S. Yang, H. Bhadeshia, *Austenite grain size and the martensite-start temperature*, Scr. Mater. 60 (7) (2009) 493–495, https://doi.org/10.1016/j.scriptamat.2008.11.043.

[93] J.-H. Liu, N. Binot, D. Delagnes, M. Jahazi, Influence of the cooling rate below Ms on the martensitic transformation in a low alloy medium-carbon steel, J. Mater. Res. Technol. 12 (2021) 234–242, https://doi.org/10.1016/j.jmrt.2021.02.075.

[94] B. Hutchinson, J. Hagström, O. Karlsson, D. Lindell, M. Tornberg, F. Lindberg, M. Thuvander, *Microstructures and hardness of as-quenched martensites (0.1–0.5% C)*, Acta Mater. 59 (14) (2011) 5845–5858, https://doi.org/10.1016/j.actamat.2011.05.061.